Identification of Myeloid Protein Kinase C – Epsilon as a Novel Atheroprotective Gene

Alexis T. Wells[1], Ramon Bossardi Ramos[2], Michelle M. Shen[1], Redwan H. Binrouf[1], Anna E. D'Amico[1], Michelle R. Lennartz[1]

[1]Department of Regenerative and Cancer Cell Biology, [2]Department of Molecular and Cellular Physiology, Albany Medical College, 47 New Scotland Avenue, Albany, New York, 12208-3479, USA

Short title: Myeloid PKCε is a Novel Atheroprotective Gene

Address correspondence to: Michelle R. Lennartz and Alexis T. Wells, 47 New Scotland Ave, Room MS-309, Albany Medical College, Mail Code 165, Albany, New York 12208-3479, USA; Telephone: 518-262-5217; e-mail: LennarM@amc.edu or wellsa2@amc.edu

Total word count: 11,444

The authors have declared that no conflict of interest exists.

BACKGROUND: Atherosclerosis is a chronic inflammatory disease driven by macrophages (MØ). Protein Kinase C – epsilon (PKCε) is a serine/threonine kinase involved in diverse cellular processes including migration, growth, differentiation, and survival. PKCε acts in a context dependent manner within the heart, however, its role in atherosclerosis is unknown.

METHODS: Bone marrow derived MØ from global PKCε knockout mice were tested for lipid retention and cytokine secretion. Public geneset analysis assessed raw counts of PRKCE in human atheromas to determine translational relevance. A LysM Cre PKCε$^{fl/fl}$ (mεKO) mouse was developed to study the impact of myeloid PKCε on atherosclerosis. After confirming myeloid selective PKCε deletion, human-like hypercholesterolemia was induced and multiple metrics of atherosclerosis were compared in WT and mεKO plaques. RNA sequencing was used to provide unbiased insight into possible mechanisms by which PKCε regulates atherosclerosis.

RESULTS: Public geneset analysis of human atherosclerotic plaque tissue revealed that PKCε expression is inversely correlated with plaque vulnerability. Similarly, peritoneal MØ from WT hypercholesterolemic mice have significantly lower PKCε expression, providing a translational rational for generation of the mεKO mouse. qPCR revealed no differences between genotypes in the expression of genes related to atherosclerosis, at either steady state or upon lipid loading, suggesting that loss of PKCε does not fundamentally change the basal state and that differences seen are a result of a more complex pathway. Comparing descending aorta and aortic root plaques

from WT and mεKO hypercholesterolemic mice revealed that mεKO plaques are larger, have larger foam cells and regions of necrosis, and thinner collagen caps. Upon lipid loading in vitro and in vivo, mεKO MØ retained significantly more cholesterol and lipid droplets than WT; Gene Ontology suggests higher expression of genes related to endocytosis in mεKO MØ compared to WT.

CONCLUSIONS: PKCε expression is decreased in vulnerable human plaques and decreases in mouse MØ upon lipid loading. mεKO plaques are larger and exhibit markers of vulnerability. With no differences in scavenger receptor (SR) expression, the impact of PKCε deletion is more subtle than simple SR dysregulation. RNA sequencing implicates higher expression of genes involved in endocytosis and mεKO MØ have significantly more lipid-containing endosomes. The data define the atherophenotype of mεKO mice and demonstrate that PKCε restricts lipid uptake into MØ by a mechanism independent of SR expression. Taken together, these studies identify PKCε as a novel atheroprotective gene, laying the foundation for mechanistic studies on the endocytic signaling networks responsible for the phenotype.

Non-standard Abbreviations and Acronyms

CVD	Cardiovascular Disease
MØ	Macrophages
LDL	Low Density Lipoprotein
Hi-ox-LDL	Highly Oxidized LDL
Ac-LDL	Acetylated LDL
LD	Lipid Droplets
MI	Myocardial Infarction
BMDM	Bone marrow derived macrophages
pMAC	Peritoneal Macrophages
PKCε	Protein Kinase C epsilon
C57BL/6	C57BL/6 Mouse Strain
εKO	Global PKCε Knockout Mouse Strain
WT	PKC$\varepsilon^{fl/fl}$ Mouse Strain
mεKO	LysM Cre PKC$\varepsilon^{fl/fl}$ Mouse Strain
AAV8-PCSK9	Recombinant Adeno-Associated Viral Vector Serotype 8 – Proprotein Convertase Subtilisin/Kexin Type 9
HFD	High Fat Diet/Western diet
OCT	Optimal Cutting Temperature Compound
ORO	Oil Red O
TNFα	Tumor necrosis factor-α
IL6	Interleukin 6
TC	Total Cholesterol
FC	Free Cholesterol
CE	Cholesterol Esters
EDTA	Ethylenediaminetetraacetic Acid
DMEM	Dulbecco's Modified Eagle's Medium
BMM	Bone Marrow Media
FBS	Fetal bovine serum
PFA	Paraformaldehyde
PBS	Phosphate-buffered saline
ANOVA	Analysis of Variance
SEM	Standard error of the mean
PCA	Principle Component Analysis
CBC	Complete Blood Count

GRAPHIC ABSTRACT:

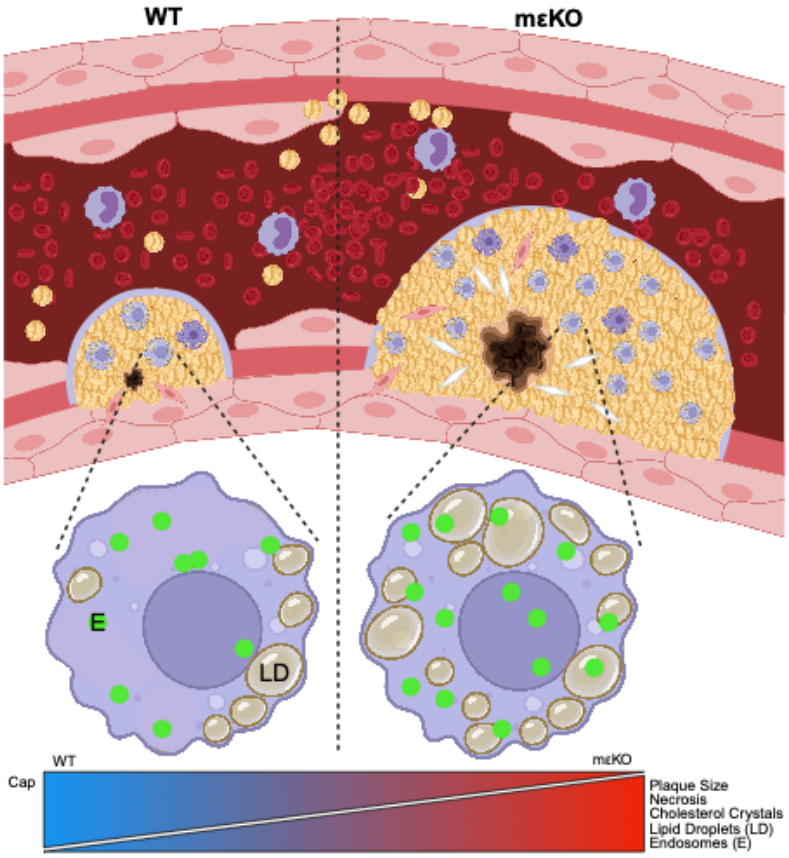

Created in BioRender. Wells, A. (2024) https://BioRender.com/ u28y100

134 **Introduction**

135 Cardiovascular disease (CVD) is the leading cause of death worldwide, with
136 atherosclerosis being a major contributor.[1,2] Despite the widespread use of statins, CVD
137 remains a major health care problem, accounting for 1 in 5 deaths in the U.S. (2022)
138 and 12% of health care costs ($378 billion in 2017-2018).[3,4] New strategies and
139 targeted therapies are needed to combat these statistics, reducing atherosclerosis and
140 the catastrophic effects (heart attack and stroke) of plaque rupture.

141 There is a cascade of events that occur during the development of atherosclerosis
142 (Figure 2A).[5,6] Macrophages (MØ) migrate to sites of endothelial damage, extravasate
143 into the intima, and internalize modified and non-modified low-density lipoprotein (LDL)
144 through scavenger receptors or LDLR. At later stages, cells within the plaque become
145 apoptotic and, if not removed by efferocytosis, contribute to the necrosis prevalent in
146 advanced plaques.[7] While plaque size may vary, the more critical factor in assessing
147 vulnerability is plaque composition.[5,6,8] That is, human vulnerable plaques have thin
148 fibrous caps, embedded collagen covered by new plaque growth, are foam cell rich, and
149 have large necrotic cores.[6,8] This constellation of factors produces chronic inflammation
150 that can result in thrombosis, leading to angina, myocardial infarction (MI), stroke, and
151 even death.[5,9,10]

152 Previously, we analyzed gene expression in human carotid and femoral plaques
153 and found that proximal regions of carotid plaques had increased expression of MØ
154 activation markers, including FcγR, SR-A1, TNFα, and PKCδ.[11] Protein Kinase Cs are a
155 family of master kinases, linked to virtually every known signaling network. Our
156 subsequent work identified protein kinase C epsilon (PKCε), a PKCδ related family

157 member, as an inflammatory signaling node.[12] Its involvement in IgG-mediated
158 phagocytosis, respiratory burst, and NF-κB activation is well documented.[4,13-21] This
159 suggests that PKCε can moderate excessive inflammation but *how* it accomplishes this
160 is a fundamental unanswered question. As atherosclerosis is a chronic inflammatory
161 disease, we investigated the role of macrophage PKCε in plaque development.

162 PKCs act in protection and pathology, depending on context.[17,22-25] PKCε has been
163 linked to inflammation in patients with atherosclerosis, hypertension-induced heart
164 failure, and conversely, to protection against ischemia-reperfusion injury and myocardial
165 infarction.[22,23,25,26] In vascular smooth muscle cells, PKCε inhibits apoptosis, increases
166 MMP-2 and -9 expression, and induces migration. [27] In cardiomyocytes, PKCε regulates
167 the interaction between conexin43 and a potassium channel subunit (Kir6.1) within the
168 mitochondria, preventing hypoxia-induced cell death.[28] In MØ, PKCε has been linked to
169 phagocytosis of aggregated LDL and resistin signaling via TLR4/MyD88, thus
170 increasing lipid accumulation and inflammation.[23,27,29,30] In contrast, a large randomized
171 clinical trial using high-dose adenosine (activator of PKCε) during acute MI found a
172 significant *reduction* in infarct size.[27,31] Thus, the role of PKCε in cardiovascular disease
173 is still an open question.

174 PKCε is perhaps best known as an oncogene, overexpressed in many cancers
175 where it enhances tumor cell migration, invasion, and resistance to apoptosis.[32-37] If
176 applied to MØ and atherosclerosis, these properties could be atheroprotective. That is,
177 PKCε may support MØ recruitment into early plaques, regulate the uptake/retention/
178 efflux of cholesterol, promote cell survival extending MØ lifetime for increased
179 efferocytosis, and protect against metrics of atherogenesis that contribute to MI and

180 heart failure. Thus, the same PKCε processes that are pathological in cancer may slow
181 the development of atherosclerosis making it a potential therapeutic target. as a
182 therapeutic agent for several diseases. Its expression at steady state may sustain
183 homeostasis but its decrease or overexpression produces pathology. Yet, the role of
184 myeloid PKCε in atherosclerosis is unknown.

185 In vivo studies indicate that loading MØ with LDL decreases PKCε expression,
186 which parallels RNAseq data from human plaques (PKCε is significantly lower in
187 advanced plaques). This would suggest that PKCε levels decrease as atherosclerosis
188 progresses and implicates PKCε in lipid handling. This hypothesis is supported by
189 studies with MØ from PKCε KO mice, which revealed that PKCε null MØ retain more
190 lipid and secrete more TNFα, both pro-inflammatory responses. To study the impact of
191 MØ PKCε in atherosclerosis, we generated PKCε$^{fl/fl}$ mice and crossed them to LysM
192 Cre, generating a myeloid specific PKCε knockout mouse (mεKO). Using the AAV8-
193 PCSK9 model to induce hypercholesterolemia in mεKO and their siblings lacking LysM
194 Cre (i.e., "wild type" with respect to PKCε expression), we applied a variety of human
195 plaque metrics. Plaques from mεKO mice were more advanced with evidence of
196 vulnerability. RNA sequencing of MØ from hypercholesterolemic WT and mεKO mice
197 suggests that PKCε regulates signaling pathways related to endocytosis, that may
198 restrict lipid retention, slowing disease progression. Taken together, this work presents
199 multiple lines of evidence implicating MØ PKCε in atheroprotection and implicates
200 endocytosis signaling as a potential mechanism.
201

202 **MATERIALS and METHODS**

203 **Sex as a Biological Variable/Limitations of the Study**

204 Atherosclerosis disproportionately affects human males vs pre-menopausal women.[38]
205 As 8-24 weeks in mice correspond to ~15-25 years in humans,[39] and mice undergo
206 changes similar to menopause at 9-12 months,[40] female mice are still cycling at 8-24
207 weeks. Thus, to maximize the chances of seeing phenotypic differences, this study was
208 limited to males. It should be noted that while males and females were included in the
209 first cohort, the females did not remain hypercholesterolemic for the 16 weeks and did
210 not produce plaques. The response of female mice to AAV8-PCSK9 strategy is reported
211 to be lower than that of males, so the virus will have to be titrated[41] to ensure long-term
212 hypercholesterolemia before determining the effect of MØ PKCε on plaque progression
213 in females.

214

215 **Reagents**

216 ACK lysis buffer: 0.5 M NH_4Cl, 1 mM $KHCO_3$, and 0.1 mM EDTA (pH 7.4). Bone marrow
217 media (BMM): DMEM containing 10% FBS, 20% L Cell media, 1% Na Pyruvate, 1%
218 Glutamax, 0.03% sodium bicarbonate, 1% nonessential amino acids, and 50 μg/ml
219 gentamicin. Cell media: BMM lacking L cell media. Sucrose lysis buffer/P^3I: 50 mM Tris-
220 HCl, pH 7.4, 0.25 M sucrose, 2.5 mM DTT, 2.5 mM EDTA, containing P^3I [5 mM
221 benzamidine, 50 mg/mL leupeptin, 50 mg/mL aprotinin, 50 mg/mL trypsin inhibitor, 5
222 mg/mL pepstatin, 1 mM PMSF, 20 mM NaF, 1 mM Na_3VO_4, 1 mM para-nitro-
223 phenylphosphate, 5 mM imidazole (Sigma)]. TBST: 5 mM Tris, pH 7.4 containing 150

224 mM NaCl and 0.1% Tween® 20. Flow buffer: PBS, 2% FBS, 2mM EDTA. Flow blocking
225 buffer: flow buffer containing 10% rat serum and 5 µg/ml 2.4G2 FcR blocking Ab).
226
227 **Publicly Available RNA-Seq Data** (**GSE1104140**)
228 The RNA-seq data was retrieved from GSE104140. Raw counts of PRKCE, as a
229 measure of unmodified gene expression, in diffuse intimal thickening (defined by AHA
230 as normal intima[42]; and advanced calcified or non-calcified fibroatheroma. Data was
231 analyzed using iDEP custom R code for differential expression (limma-voom). Principle
232 component analysis (PCA) emphasizes the variation between groups as well as the
233 similarities within each group.
234
235 **Insoluble Immune Complexes**
236 10 µl of 10 mg/mL BSA (Sigma A0281) was added to 300 µl of 2 mg/mL rabbit anti-BSA
237 IgG (Sigma, B1520) in Optimem™ buffer (ThermoFisher Scientific, 31985070).
238 Complexes formed by rotation (1 hour, 37°C). Complexes were pelleted and washed
239 twice with Optimem, and resuspended to the initial volume. 15 µl of this stock solution
240 was added/1 x 10^6 BMDM.
241
242 **Mice**
243 All animal procedures were approved by the Albany Medical Center Institutional Animal
244 Care and Use Committee protocol #1903003 and #2204004 (breeding) and #2304003
245 (AAV8 and high fat diet). Cells from both males and females were used for *in vitro*
246 studies; there were no effects of sex or age (3-6 months) on experimental outcome.

247 Cells obtained from one mouse represent one independent experiment. All animals/cells
248 were identified by ear-tag (not genotype) to minimize unconscious bias. The lab
249 manager identified animals to be used in each experiment. Genotypes were revealed
250 after all data was collected.
251
252 **Global PKCε Knockout Mice (εKO)**
253 PKCε$^{+/-}$ heterozygotes on the C57BL/6 background were purchased from Jackson
254 Laboratory (*B6.129S4-Prkce^{tm1Msg}/J* stock# 004189; Bar Harbor, ME) and bred in the
255 Albany Medical Center Animal Resources Facility. Mice were fed a standard chow,
256 housed under regular 12/12 light-dark cycles at a temperature of 20-26°C, and a
257 humidity level of 20-70%. Global deletion of PKCε in mice leads to noticeably smaller
258 offspring with an immunodeficiency causing εKO mice to succumb to infections and fall
259 out of lineage. Heterozygotes were crossed to produce the wild-type (C57BL/6) and
260 PKCε$^{-/-}$ (εKO) siblings.
261
262 **Myeloid Selective PKCε Knockout Mouse (mεKO)**
263 PKCε$^{fl/fl}$ mice were generated by IVF at Taconic Labs (Germantown, NY) from sperm
264 provided by The Genome Editing and Animal Models Core at the University of
265 Wisconsin (Madison) Biotechnology Center. This C57BL/6 congenic strain was
266 deposited at The Jackson labs (B6(Cg)-*Prkce$^{tm1.1Akv}$*/LennMmjax stock# 69556). PKCε$^{fl/fl}$
267 females were then crossed to LysM Cre males (Jackson Laboratory, Strain #004781
268 B6.129P2-*Lyz2$^{tm1(cre)Ifo}$*/J) to produce LysM Cre$^{+/-}$ PKCε$^{fl/fl}$ pups. To maintain the colony
269 PKCε$^{fl/fl}$ females were crossed to LysM Cre$^{+/-}$ PKCε$^{fl/fl}$ males to produce PKCε$^{fl/fl}$

270 offspring, some of which lacked LysM Cre (designated WT) and siblings expressing
271 hemizygous LysM Cre (**m**yeloid selective PKCε **k**nock**o**ut, designated mεKO). A subset
272 of this colony carried the ZsGreen Cre reporter gene (B6.Cg-*Gt(ROSA)26Sor*$^{tm6(CAG-}$
273 $^{ZsGreen1)Hze}$/J maintained as heterozygous) and was used to confirm specificity of Cre
274 expressing MØ in mεKO plaques [as well as in blood (neutrophils and MØ) and
275 splenocytes (B and T cells). Zs green carrying animals are indicated by green symbols
276 on graphs; expression of ZsGreen had no impact on plaque metrics. Mice were fed a
277 standard chow, housed under regular 12/12 light-dark cycles at a temperature of 20-
278 26°C, and a humidity level of 20-70%. Compared to the parental C57BL/6 strain, there
279 are no obvious size, behavioral, or health issues with either the WT or mεKO animals or
280 in animals carrying/expressing the ZsGreen gene.
281
282 **Generation of Hypercholesterolemic Mice**
283 Cohort animals were identified and their eartags recorded. Weights of 8-week-old mice
284 were recorded at the time of retro-orbital injections of AAV8-PCSK9 ($1x10^{12}$ gc/200 µl
285 sterile PBS). Animals were given a high fat (HFD, "Western") diet (Inotiv, TD.88137) for
286 4 or 16 weeks. At two weeks post-injection/HFD, and at the time of sacrifice, blood was
287 collected (submandibular bleed or portal vein pull) for plasma cholesterol
288 measurements (Fujifilm Healthcare Americas Corp Cholesterol E kit, NC9138103); ≥500
289 mg/dL was considered hypercholesterolemic. mεKO mice are indistinguishable from
290 their WT counterparts. Breeding LysMCre hemizygote studs to LysMCre negative dams
291 produced litters of 7-13 animals that were approximately 50% LysMCre$^{+/-}$ making it

292 relatively easy to generate sufficient numbers of each genotype for the atherosclerosis
293 cohorts.
294 The final experimental conditions were chosen from the results of a pilot
295 experiment. Pilot experiments: 16 mice (8 male, 8 female; two timepoints 9- and 16-
296 weeks post AAV8/HFD). Females had high plasma cholesterol at 2 weeks that
297 decreased over time. Males remained hypercholesterolemic for the duration. At 9
298 weeks, no animals had visible plaque. At 16 weeks, males, but not females, had
299 developed plaques. The lack of plaques in females correlates with their lack of
300 sustained hypercholesterolemia due to the AAV8-PCSK9 model dosage. Thus,
301 subsequent cohorts were male only, harvesting cells 4 weeks and tissue 16 weeks after
302 AAV8/HFD.
303
304 **Elicited Peritoneal MØ (pMACs)**
305 Mice were injected i.p. with 3 mL sterile 3% Thioglycolate solution. Animals were
306 euthanized after four days and pMACs recovered by peritoneal lavage with 10mL PBS
307 and red blood cells removed via ACK lysis.
308
309 **Bone Marrow-derived MØ (BMDM)**
310 Differentiated macrophages were derived from bone marrow stem cells as previously
311 described.[12] Briefly, mice were euthanized via isoflurane and cervical dislocation.
312 Femurs and pelvises were removed and flushed for bone marrow collection. Red blood
313 cells were lysed with ACK lysis buffer and the recovered stem cells were differentiated
314 in BMM. BMDM were used 7-9 days after harvesting.

315

316 **ELISA assays**

317 C57BL/6 and εKO BMDM (1.5 x 10^6/well, 6 well plate) were incubated with or without
318 immune complexes for 2 hours. Culture media was collected and IL6 and TNFα was
319 quantified using BioLegend ELISA Max™ kits (431301 and 430901) per the
320 manufacturer's instructions. Results are reported as as pg/mL net release.

321

322 **Western Blotting**

323 Brains were homogenized (sucrose lysis buffer/P^3I) using a KINEMATICA Polytron PT
324 10 20 3500 115v. The homogenate was sonicated on ice 2 x 10 s (Sonics & Materials
325 Vibra-cell VC High Intensity Ultrasonic Processor) and centrifuged (13,000 x g, 10
326 minutes, 4°C) to remove particulates. 3 µg of protein (Bradford Assay) was used for
327 western blots. Spleens were minced in PBS and passed through a 70 µm cell strainer
328 (CELLTREAT, 229483). Erythrocytes were ACK lysed and splenocytes recovered by
329 centrifugation (400 x g, 10 minutes, 4°C). Splenocytes were solubilized in 400 µl
330 sucrose lysis buffer, followed by sonication on ice (2 x 10 s). After clarification by
331 centrifugation (13,000 x g, 10 minutes, 4°C), protein was quantified (Bradford Assay);
332 100 µg was loaded/lane. BMDMs and pMACs were suspended in 100 µl Sucrose Lysis
333 Buffer/P^3I, and sonicated for 7 s on ice. Samples were clarified by centrifugation (13,000
334 x g, 10 min 4°C), and protein was quantitated; 300 µg of protein/lane was used for
335 western blots.

336 Proteins were separated on a 10% PAGE under reducing conditions. The Bio-Rad
337 Precision Plus Protein Kaleidoscope ladder (1610375) served as the molecular weight

338 standards. Gels were transferred onto a PVDF membrane using an iBlot® system.
339 Membranes were blocked with 5% milk in 1X TBST (1 hour) and washed 3 times with
340 TBST. Antibodies were diluted in 3% BSA/TBST (Major Resources Table) and allowed
341 to bind overnight (4°C with rocking); GAPDH served as the loading control. The
342 following day, membranes were washed 5 times with TBST, probed with an HRP
343 secondary antibody (1:10,000 in 3% BSA/TBST, Major Resources Table) for 1 hour RT
344 while rocking. Membranes were washed (5 times with TBST) and developed using Bio-
345 Rad's Clarity Western ECL Substrate kit (1705060) according to the manufacturer's
346 instructions. Membranes were imaged using a Bio-Rad ChemiDoc™ MP Imaging
347 System. Densitometry was used to quantify genotype differences in PKC expression.
348 TIFF files were opened in FIJI and the Analyze → Gels function was used to generate
349 peaks to the corresponding bands. Peaks were separated and the wand tool used to
350 quantify the area of each band. For each band the background was subtracted,
351 normalized to GAPDH and their WT counterparts. Fold change relative to C57BL/6 or
352 WT was reported.
353
354 **Blood Collection for Complete Blood Count (CBC)**
355 Blood was collected from mice via the portal vein into 1mL syringes containing 100 µl
356 heparin. CBC analysis was performed using a Heska ElementHT5 Veterinary
357 Hematology Analyzer (Heska Corporation, Loveland, Colorado). The percent
358 composition of total white blood cells was calculated and reported. The total number of
359 circulating RBC, WBC, lymphocytes, monocytes, neutrophils, eosinophils, and basoplils
360 were collected and reported as Cells (10^6/µl).

361

362 **qPCR**

363 RNA from $1x10^6$ MØ were extracted with PureLink™ RNA Mini Kit (ThermoFisher
364 Scientific, 12183018A); RNA purity and concentration was determined by Nanodrop.
365 RNA was reversed transcribed using qScript cDNA SuperMix (QuantaBio, 95048-500).
366 cDNA was then used for qPCR. Each 20 µl reaction contained 10 µl Quanta PerfeCTa
367 Syber Green Fast Mix (QuantaBio, 95071-012), 8 nMol of forward and reverse primers
368 (Origene), and 50 ng cDNA. Thermocycler Ct values were exported into an Excel file
369 and the relative expression ($2^{-\Delta Ct}$) was calculated and reported. All samples were
370 normalized to β-actin (see Major Resources Table for primer sequences).

371

372 **Flow Cytometry**

373 50 - 100 µl of BMDM or pMAC (at 1×10^7/mL) were blocked (30-60 min, ice) before
374 antibody staining (45 min, ice in the dark; Major Resources Table). After staining, cells
375 were resuspended in 500 µl of flow buffer and read on a Bio-Rad ZE5 Cell Analyzer
376 driven by Everest software. Data was analyzed with FlowJo 10.10.

377

378 **In Vitro Lipid Loading**

379 *Human highly-oxidized-LDL* (Kalen Biomedical, #770252)*:* $5x10^5$ BMDM were incubated
380 with 50 µg/mL ox-LDL (24 hours, complete media), washed with PBS, and processed
381 for flow cytometry, cholesterol retention, or western blotting.

382 *Ac-LDL* (ThermoFisher Scientific, #L23380): 5.0 x 10^5 BMDM were incubated with 5
383 µg/mL A488 Acetylated LDL (30, 60 minutes, complete media), washed with PBS,
384 resuspended in flow buffer for flow cytometery.
385
386 **Quantitation of Lipid Droplets in BMDM from Global PKCε Knockout (εKO) Mice**
387 Initial studies (Figure 1) were done using BMDM from the global PKCε knockout mice
388 (εKO). 5.0 x 10^4 C57BL/6 or εKO BMDM were plated on coverslips in 24 well plates.
389 Acetylated LDL (Kalen BioMedical, 770201-6; 360 µg/mL in BMM) was added. After 4
390 hours, the cells were washed with PBS and fixed (4% PFA, 15 min, RT). Coverslips
391 were washed with PBS, stained with BODIPY (ThermoFisher Scientific, D3922, 30 min)
392 and mounted. Z stacks were collected, 3-D reconstitutions were made, and droplet
393 number and area was quantified using Imaris® software.
394
395 **Quantitation of Cholesterol Retention**
396 BMDM were lipid loaded (24 h, ox-LDL), washed and held at -80°C until analyzed. Total
397 and free cholesterol was quantified from the cell lysates using the Cholesterol Ester-
398 Glow^{TM} kit (Promega, J3190) according to the manufacturer's instructions. Data was
399 normalized to the total amount of protein collected from cell lysates. Technical replicates
400 were averaged, and cholesterol ester content calculated as the difference between total
401 and free cholesterol.
402
403 **Lipid Droplet Quantitation in Foam Cells**

404 Four weeks after induction of hypercholesterolemia, elicited pMACs were harvested,
405 resuspended in Dulbecci's modified Eagle's medium (DMEM) and adhered in 8-well
406 chamber slides (Falcon, 354108) (30 minutes). Lipid droplets were visualized with
407 LipidTOX (Invitrogen, H34476; 1:100) (30 minutes, RT) and mounted using ProLong
408 Glass Antifade Mountant with NucBlue (Invitrogen, P36981). Merged images were
409 created using FIJI software.
410
411 **Tissue Collection and Processing**
412 Studies were terminated by isoflurane euthanasia and cervical dislocation. Blood was
413 collected from the portal vein for plasma cholesterol determination. Animals were
414 exsanguinated with 10 mL warm PBS through the left ventricle using a syringe and 25-
415 gauge needle at constant pressure. Hearts and aortic arches/descending aortas were
416 collected.
417 Descending aortas were collected from the base of the ascending aorta to the
418 common iliac artery, keeping the branches of the brachiocephalic, left common carotid,
419 and left subclavian arteries intact. Aortas were fixed (4% PFA overnight, RT) and stored
420 at 4°C in PBS/Thimerosal. *En face* preparations were made by opening the lumen,
421 pinning the tissue flat, and staining with 0.3% ORO (15 minutes, RT). After staining,
422 arches were washed with 70% EtOH for 1 minute followed by 2 washes of 1X PBS for 5
423 minutes. Tissue area was defined by the aortic arch and 3 mm of the descending aorta
424 (no plaque was present beyond 3 mm). Plaque area was quantitated in FIJI using the
425 color thresholding macro and normalized to tissue area. The percent lesion coverage
426 was reported.

427 For aortic roots, hearts were cut parallel to the tip of the atria. The upper half,
428 containing the aortic root was placed in a cryomold containing optimal cutting
429 temperature compound (OCT) and held at -80ºC until sectioned. A total of 25 charged
430 slides with 3-4 10 μm thick sections per slide were collected from each mouse as
431 previously described.[43] Briefly, sequential sections were put on individual slides, such
432 that sections 1 to 25 went on slides 1 to 25. Sections 26 to 50 were placed on slides 1
433 to 25, respectively, and so on. This generated 25 slides, each containing multiple
434 sections separated by ~250 μm and spanning the entire plaque length. Six slides (e.g.
435 Slides 1, 5, 9, etc.) were chosen for H & E staining. Contiguous slides (e.g. 2,6,10, etc.)
436 were stained with ORO. Sirius red staining was done on serial slides (e.g. 3,7,11, etc.)
437 and the next slides in the series (e.g. 4,8,12, etc.) for F4/80. This strategy produced
438 multiple datapoints (6 slides x multiple measurements per slide) for each plaque feature,
439 with contiguous slides allowing for visualization of different features in close proximity.
440

441 **H&E Staining and Analysis**

442 To quantify lesion size and necrosis, 6 slides (see above) were chosen, with the first
443 beginning at the base of the aortic root (the first site of plaque deposition). Fresh tissue
444 sections were fixed for 3 minutes in a solution comprised of 100% EtOH, 40% PFA,
445 100% Glacial acetic acid, and diluted with diH_2O to make a 4% PFA solution. Fixed
446 sections were dehydrated in 70% EtOH followed by 95% EtOH (1 minute), washed in
447 running tap H_2O and diH_2O (30 s), stained with Hematoxylin (4 minutes), and washed
448 with tap H_2O until clear. Stained samples were then clarified for 15 seconds, washed
449 with tap H_2O, placed in bluing agent for 1 minute and then washed with tap H_2O. After

450 Hematoxylin staining, tissues were placed in 95% EtOH followed by Eosin-Y stain for 15
451 s each. To wash away excess Eosin samples were placed in multiple changes of 95%
452 EtOH (x2) and 100% EtOH (x3) for 1 minute each. Tissues were cleared in xylene,
453 mounted in Cytoseal XYL, and left to dry overnight prior to imaging. Images were
454 analyzed with NDP.view 2 software. The lesion and necrotic regions were outlined, and
455 the areas were recorded. Areas were then averaged between sections of the same
456 mouse and the average lesion area per mouse was reported. Percent necrosis was
457 then calculated by dividing the necrotic area by lesion area per mouse.
458
459 **ORO Staining and Analysis**
460 Sections consecutive to those stained with H&E were taken to quantify average foam
461 cells size. Slides were fixed (4% PFA, 10 minutes), washed, and dried with 60%
462 isopropyl alcohol. Sections were stained with 0.3% ORO (20 minutes), rinsed with H_2O,
463 counter-stained with Hematoxylin (1 minute) and mounted in Gelvatol. Slides were
464 imaged within 24 hours of staining. Images were analyzed with NDP.view 2 software.
465 Regions of foam cells were measured for area and divided by the number of nuclei
466 within that area (number of nuclei obtained from H&E sections). This was performed at
467 3-5 regions on all sections, averaged for each mouse and reported as average foam cell
468 size/animal.
469
470 **Sirius Rred Staining and Analysis**
471 Consecutive sections to those stained with ORO were taken to quantify cap thickness
472 and percent collagen. Slides were fixed in 70% EtOH for 3 minutes, washed with diH_2O

473 and stained in 0.1% Sirius red/Direct 80 saturated in an aqueous solution of picric acid
474 (1 hour, room temperature). Tissues were washed (2 x 0.5% acetic acid, 5 minutes),
475 dehydrated in 100% EtOH and cleared with xylene. Slides were mounted with Cytoseal
476 XYL and dried overnight prior to imaging. Images were analyzed with FIJI software. The
477 percent collagen content was calculated by normalizing the collagen area to the lesion
478 area and was reported per mouse. The plaque cap thickness was taken from 3-5
479 regions along each plaque and averaged per section. If no cap was present, then the
480 thickness was recorded as 0. Average cap thickness was then divided by the lesion
481 area and was reported per mouse. The thickest and thinnest cap regions were then
482 extracted and assessed for genotype differences.
483
484 **RNA Ssequencing** (**GSE291828**)
485 8 week-old WT and mεKO mice were administered with AAV8-PCSK9 and given a
486 chow or Western diet (as previously described) for 4 weeks and elicited pMACs were
487 harvested. RNA was isolated from each mouse using TRIzol (Invitrogen, 15596026)
488 according to manufacturer instructions. Sequencing was done as previously described,
489 but with the mm10 gemone.[44] Briefly, all RNA samples passed quality control (>8.6 RIN)
490 and the RNA library was performed using the polyA selection method. RNA samples
491 were sequenced by GENEWIZ using the illumina HiSeq system in a 2 x 150-bp
492 configuration. Files were trimmed using Trim Galore (GitHub repository,
493 https://github.com/FelixKrueger/TrimGalore) and aligned/annotated with Rsubread's
494 v1.5.3 to the mm10 genome. Genes above 0.5 counts-per-million in at least 3 samples
495 were kept in the analysis. Differential expression analysis was performed using limma-

496 voom and significance was defined as *P* value < 0.05. Principal component analysis
497 (PCA) indicates a distinct gene expression profile between conditions using R.
498 Functional enrichment analysis was performed using WebGestalt
499 (https://www.webgestalt.org/), and Metascape (version 3.5). Notably, between WT and
500 mεKO atheroprone mice (AAV8-PCSK9 + Western diet/HFD), Gene Ontology revealed
501 the *Import Into Cell* GO family of differentially regulated genes was within the top 20 GO
502 families. This family includes genes related to phagocytosis, endocytosis, and receptor-
503 mediated endocytosis. From which, a heatmap was generated using raw counts in R.
504

505 **Imaging**

506 Lipid loaded C57BL/6 and εKO BMDM*:* Cells were imaged on an Olympus IX81-DSU
507 spinning-disc confocal microscope at 60X oil with a Hamamatsu electron multiplying
508 charge-coupled device camera, driven by MetaMorph software (Molecular Devices,
509 Sunnyside, CA). Raw images were then processed using Imaris Software. Aortic
510 arches. Olympus SZ61 Dissecting Microscope equipped with an HD camera & monitor
511 system from Excelis HDS was used to acquire images of aortic arches. Raw images
512 were processed with FIJI software. Aortic root: H&E, ORO, and Sirius red images were
513 aquired on a high-Speed, High-resolution Digital Slide Scanner. Hamamatsu
514 NanoZoomer 2.0RS. Images were collected with a 40X air objective. F4/80 images
515 were aquired on an Olympus BX51 microscope (Olympus, Tokyo, Japan) equipped with
516 a QImaging Retiga 2000R digital camera (QImaging, Surrey, British Columbia, Canada)
517 and CellSens software (Olympus Life Science, Waltham, MA). Images were collected
518 with a 40X air objective. Raw images were processed with NDP.view 2 or FIJI software.

519 *In vivo lipid loaded WT and mεKO pMAC*. Images were aquired on an Olympus
520 BX51 microscope (Olympus, Tokyo, Japan) equipped with a QImaging Retiga 2000R
521 digital camera (QImaging, Surrey, British Columbia, Canada) and CellSens software
522 (Olympus Life Science, Waltham, MA). Images were collected with a 40X air objective.
523 Raw images were processed with FIJI software.
524
525 **Statistics**
526 All experiments were conducted in a blinded fashion using ear-tags for identification.
527 Once all data was analyzed, the code was broken to run statistics. Data are expressed
528 as mean ± SEM of independent experiments or animals; *n* is noted in the figure
529 legends. Limma-voon was used to assess differential expression. Comparison of means
530 between groups was evaluated by one-way ANOVA or two-way ANOVA with Tukey
531 multiple comparisons, 2-tailed paired or unpaired students t-test, or Mann-Whitney U
532 test. Bland-Altman test was used for interobserver variability. A p-value less than 0.05
533 was considered statistically significant. All statistical analyses were performed using
534 GraphPad Prism, SPSS, and R. Representative images were chosen based on those
535 closest to the mean.
536
537 **Study Approval**
538 All animals received humane care in accordance with the NIH Guide for the Care and
539 Use of Laboratory Animals. All procedures were approved by the Albany Medical Center
540 Institutional Animal Care and Use Committee protocol #1903003 (εKO breeding),
541 #2204004 (mεKO breeding), and #2304003 (WT and mεKO AAV8 and high fat diet).

542

543 **Data Availability**

544 The public geneset data used to assess PRKCE read counts in early and advanced
545 stages of atherosclerosis can be found on NCBI under GSE104140. RNA sequencing
546 performed for this manuscript can be found on NCBI under GSE291828. Please see the
547 Major Resources Table in the Supplemental Materials.

548

549 **RESULTS**

550 *εKO BMDM and a human atheroma RNAseq dataset suggest PKCε may be*
551 *atheroprotective, regulating lipid dynamics*. Based on our work demonstrating the role of
552 PKCε in vesicular trafficking and FcR-mediated phagocytosis,[12] we hypothesized that
553 PKCε is involved in the uptake of modified lipids. To test this, we incubated bone
554 marrow-derived macrophages (BMDM) from wild type (C57BL/6) and global PKCε
555 knockout (εKO) mice with acetylated LDL (acLDL) and quantified lipid droplet number
556 and area. εKO BMDM contained significantly more, and larger, lipid droplets, implicating
557 PKCε in lipid handling (Figure 1A). Secondly, we know that the vulnerable regions of
558 human carotid plaques have elevated expression of Fc receptors (FcR) and TNFα, that
559 PKCε is activated upon FcR ligation, and that MØ treated with oxLDL-immune
560 complexes become foam cells.[11,45] The impact of PKCε expression on cytokine release
561 is unknown. Thus, we treated C57BL/6 and εKO BMDM with immune complexes (to
562 mimic the uptake of immune complexes present at high levels in humans with
563 atherosclerosis) and quantified release of TNFα and IL6, two cytokines linked to
564 atherosclerosis.[46,47] Surprisingly, we found that secretion of TNFα, but not IL-6, was

565 significantly *higher* in εKO cells (Figure 1B,C). This suggests that PKCε restricts TNFα,
566 but not IL-6 release. That MØ lacking PKCε retain more lipid and release more TNFα
567 suggests that PKCε limits foam cell formation and restricts the release of inflammatory
568 cytokines, properties that could be protective, effectively slowing atherosclerosis
569 progression.

570 To assess the translational potential of our (mouse) results, we searched for human
571 plaque datasets but found none reporting protein expression. However, PRKCE (PKCε
572 gene) raw counts were extracted from GSE104140, a curated RNAseq dataset obtained
573 from carotid endarterectomy tissue that includes compares diffuse intimal thickening,
574 ("stage 0", a preclinical control[48,49], n=9) with two types of late stage plaques, calcified
575 (n=9) and soft atheromas (n=14) . Raw counts were used because they provide the
576 most basic and unbiased representation of gene expression. The principle component
577 analysis (PCA) demonstrates the differential expression patterns of atheromas between
578 each group as well as the similarities within each group (Figure 2B). Using R, raw
579 counts of PRKCE per person were plotted and assessed for statistical differences.
580 Compared to diffuse intimal thickening, advanced plaques have significantly lower
581 PRKCE counts. While there was no statistical difference between the calcified and soft
582 atheromas, counts trend lower in the advanced soft plaque, suggesting that PKCε
583 expression is inversely correlated with plaque stage (Figure 2B).[50]

584 Given that PKCε null MØ retain more lipid, and advanced human plaques have
585 lower PKCε expression, we asked if MØ from hypercholesterolemic mice have lower
586 PKCε. The AAV8-PCSK9 plus Western diet strategy was used for inducing
587 hypercholesterolemia[51]; control animals received AAV8-PCSK9 but were fed chow.

588 Elicited pMACs were harvested 4 weeks after AAV8 injection and PKCε expression
589 quantified by PCR. Compared to chow fed, PKCε expression was significantly lower in
590 pMACs from HFD mice (Figure 2C). To test the hypothesis that lipid loading decreases
591 PKCε protein,we quantified PKCε expression in control MØ (no lipid) and foam cells
592 produced upon incubation with highly oxidized low-density lipoprotein (Hi-ox-LDL); lipid
593 loading decreased PKCε protein levels by ~ 73 ± 2% (n=2, Figure 2D). Thus, looking at
594 mouse and human, mRNA and protein, we see a consistent decrease in PKCε in
595 advanced plaques and hypercholesterolemic MØ, suggesting that the presence of PKCε
596 in MØ limits lipid retention and, possibly, development of atherosclerosis. Testing this
597 required a mouse in which PKCε is selectively deleted from myeloid cells, an mεKO
598 mouse.

599 *LysM Cre deletes PKCε from Macrophages*. We generated a PKCε$^{fl/fl}$ mouse[52] and
600 crossed it to LysM Cre. LysM Cre deletes flox'd genes in the myeloid lineage, primarily
601 macrophages and neutrophils, with little to no effect on the lymphoid lineage.[53] PKCε$^{fl/fl}$
602 dams were mated with LysM Cre$^{+/-}$ PKCε$^{fl/fl}$ studs to produce PKCε$^{fl/fl}$ siblings that were
603 LysM Cre negative or hemizygous (Figure 3A).

604 To determine the efficiency of myeloid deletion, we compared PKCε protein
605 expression across four mouse strains: C57BL/6 (parental, all cells positive), global
606 PKCε knockout (εKO, all cells negative[54]; PKCε$^{fl/fl}$ (designated WT, theoretically all cells
607 positive), and LysM Cre$^{+/-}$ PKCε$^{fl/fl}$ (designated mεKO: **m**yeloid selective PKC**ε**
608 **k**nock**o**ut).[12] Brains and spleens were used as controls; brain because PKCε expression
609 is highest in this tissue and spleens because the majority of cells are lymphoid so PKCε
610 expression should not be affected by LysM Cre. As predicted, PKCε was expressed in

611 brains and spleens of C57BL/6 mice but was undetectable in their εKO counterparts
612 (Figure 3B). PKCε expression in WT and mεKO brains and spleens was not significantly
613 different from C57BL/6 (Figure 3B) nor was mεKO expression significantly different from
614 WT (i.e., PKCε$^{fl/fl}$). These results confirm the myeloid selectivity of LysM Cre deletion in
615 the PKCε$^{fl/fl}$ background (Figure 3B) and validate the specificity of the PKCε antibody.
616 With respect to the efficiency of PKCε deletion in MØ: BMDMs from mεKO mice had
617 no detectable PKCε; expression in mεKO pMACs was reduced >85% compared to WT,
618 a level not statistically different from mεKO BMDMs (Figure 3C,D). In conclusion, PKCε
619 expression in mεKO brains and spleens is similar to the parental C57BL/6 tissues. In
620 contrast, PKCε in mεKO MØ is low/not expressed.
621 *Characterization of mεKO mice.* Complete blood counts of WT and mεKO blood
622 revealed no differences in total numbers of circulating red blood cells (RBC), white
623 blood cells (WBC), lymphocytes, monocytes, neutrophils, eosinophils, or basophils
624 (Figure 3E-L). These results parallel the more extensive immune cell analysis done on
625 the global PKCε knockout mice (i.e., no differences in number or activity of any immune
626 cell type.[54] Additionally, we found no differences in the number of stem cells harvested
627 from bones, the number of BMDM differentiated from WT and mεKO stem cells (p=0.76,
628 n=6), or the number of elicited pMACs recovered from WT and mεKO (p=0.66, n=3),
629 Finally, we found no differences in expression of FcγR, CD11b, MHCII and Ly6C
630 between mεKO and WT BMDM, suggesting that PKCε deletion does not alter MØ
631 polarization (Supplemental Figures S1, S5D). These data suggest that, at steady state,
632 deletion of myeloid PKCε has no substantive effect on the immune system.

633 To determine the effect of PKCε deletion on other PKCs, we compared their relative
634 expression levels in BMDMs. Expression of PKC α, β, δ, η, and ζ were not significantly
635 different by PCR or western blotting (Figure 4 A-G). Thus, there is no obvious
636 compensation for PKCε in mεKO MØ. Additionally, the unique substrate specificity of
637 PKCε.[15,51,54,55] would make functional compensation difficult.

638 *Deletion of PKCε does not affect expression of key atherosclerotic and inflammatory*
639 *mediators*. Since εKO BMDMs retained more and larger lipid droplets and released
640 more TNFα (Figure 1), a likely explanation could be differential expression of scavenger
641 receptors and/or a more polarized phenotype. qPCR of BMDM, elicited pMAC, and lipid
642 loaded BMDM was used to determine the effect of PKCε deletion on the expression of
643 25 genes linked to atherosclerosis.[56] Surprisingly, there were no statistical differences in
644 message levels for any of the markers tested (Figure 5, Supplementary Figure S2-6).
645 Similary, surface expression of scavenger receptors (SR-A1, SR-E2, SR-B2, SR-E1,
646 SR-E2, and SR-B1) and pattern recognition receptors TLR 2 and 4 did not change with
647 genotype or upon lipid loading (Figure 5, Supplementary Figure S2). Thus, any
648 differences in plaque phenotype is more likely due to MØ PKCε signaling than intrinsic
649 effects of differential receptor expression.

650 *Plaques from hypercholesterolemic mεKO mice are more advanced than WT.*
651 Knowing that MØ lacking PKCε retain more lipid (Figure 1A) and release more TNFα
652 (Figure 1B), we hypothesized that loss of myeloid PKCε would exacerbate
653 atherosclerosis *in vivo* (ie, PKCε expression is protective). AAV8-PCSK9 injections plus
654 Western diet strategy[57] was used to induce human-like hypercholesterolemia and
655 plaques after 16 weeks (T=16, Figure 6A) Weight was recorded at the start of the

656 experiment and prior to tissue harvesting (T =0 and 16 weeks). While weight increased
657 with time, there were no significant genotype differences (Figure 6B). Likewise, plasma
658 cholesterol (taken at weeks 2 and 16) increased with time but there were not genotype
659 differences (Figure 6C); ≥500mg/dL of cholesterol was defined as hyper-
660 cholesterolemic.[58]

661 Standard metrics of atherosclerosis include plaque area, foam cell content, amount
662 of necrosis, and collagen cap thickness. Plaque area was measured in both the arotic
663 root and aortic arch while quantitation of foam cell number, necrotic area and cap
664 thickness was scored for arotic roots.

665 Lesion area in the aortic arch was quantified by Oil red O staining and normalized to
666 arch area as detailed in Methods. Percent lesion coverage was significantly higher in
667 mεKO aortic arches compared to WT, indicative of a higher plaque burden (Figure
668 7A,C). To test for inter-observer variability, two observers quantified a subset of the
669 aortic arches; no significant variability was found (Figure 7B).

670 The aortic root lends itself to more detailed analyses. Sections were collected at the
671 first sign of plaque near the aortic valve and sectioned such that each slide contained 3
672 x 10 μm sections at levels 250 μm apart (details in Methods). Six slides containing
673 sections closest to the center of valves were stained with Hematoxylin and Eosin (H&E).
674 Consecutive slides were stained for ORO, followed by Sirius red, followed by F4/80.

675 Lesion area and percent necrosis was quantified from H & E stained slides and
676 recapitulated the results of the aortic arches in that the aortic root lesion area was
677 significantly larger in mεKO than WT. Necrotic area, as defined by H&E dull/devoid of
678 nuclei, was significantly larger inmεKO plaques (Figure 8A). Finally, we noted

679 cholesterol clefts present in mεKO plaques;few were apparent in WT plaques (Figure
680 8A). While difficult to quantify, embedded cholesterol crystals are a hallmark of
681 advanced human plaques. [59,60]

682 Consecutive slides were stained with ORO to assess lipid retention. ORO rich areas
683 were quantified, normalized to the number of nuclei (obtained from the contiguous H&E
684 stained section), and reported as average foam cell area per mouse. Consistent with
685 the larger plaque area, mεKO plaques have larger foam cells (Figure 8B). Larger foam
686 cells would imply more retained lipid, providing in vivo validation of the in vitro lipid
687 loading of PKCε negative MØ shown in Figure 1A. These data support the hypothesis
688 that PKCε plays a role in lipid handling.

689 Consecutive slides were stained with Sirius red to visualize collagen. Overall
690 content was quantified and normalized to lesion area. Surprisingly, there was
691 significantly *more* collagen in mεKO lesions compared to WT (Figure 8C). However,
692 closer examination revealed that while collagen overlayed the foam cells in WT, much
693 of it was buried in mεKO samples. We previously reported buried collagen in carotid
694 mouse plaques[43], a metric that was used as one criteria to stage murine carotid
695 plaques. “Buried” fibrosis is also seen in human plaques and is consistent with a
696 previous disruption (i.e., instability).[61] Thus, vulnerable plaques could have more
697 collagen but with thinner caps. Larger and more necrotic plaques with little to no cap are
698 indicators of vulnerability in humans; rupture is less likely if the soft necrotic core is
699 protected by a thick fibrous cap. Applying this metric, we found significantly thicker
700 collagen caps in WT plaques; many mεKO plaques had regions with *no* cap (Figure
701 8C). Notably, a plaque is only as stable as its thinnest cap, therefore we assessed the

702 thickest and thinnest plaque cap per mouse. There were and found no differences in the
703 thickest cap regions. In contrast, mεKO plaques have significantly thinner caps than
704 their WT counterparts (Figure 8C).

705 Knowing MØ release MMPs that degrade the fibrous cap, and that MMPs 8, 9, and
706 12 are significantly upregulated in the inflamed regions of human plaques, we asked if
707 MØ are the cells overlaying the collagen in mεKO plaques.[62] To do this, we exploited
708 the availability of Jackson Laboratories **RCL-**ZsGreen reporter mouse and introduced
709 this gene into some individuals in the mεKO colonly; cells with an active LysM Cre gene
710 will be green. All the BMDM and pMACs from mεKO mice expressed ZsGreen while
711 their siblings lacking Cre did not (Figure S7B). Knowing that ZsGreen does not alter
712 plaque metrics (Figure 8) and mεKO MØ do not express PKCε (Figure 3C,D), we asked
713 if the cells overlaying collagen were F4/80 positive (i.e., MØ). Plaques from ZsGreen$^{+/-}$
714 mεKO and WT were stained for F4/80. We found co-localization of ZsGreen and F4/80
715 in mεKO but not WT mice (where Zs isn't expressed), confirming that the cells
716 overlaying collagen in mεKO plaque are PKCε null MØ (Supplemental Figure S7A).

717 *Lipid loaded MØ from mεKO mice retain more cholesterol*. Histologically, mεKO
718 plaques have larger foam cells than WT (Figure 8B). Also, we know that εKO BMDM
719 retain more lipid than their C57BL/6 counterparts (Figure 1A). Given this information, we
720 asked if mεKO MØ have a lipid handling defect. To test this, WT and mεKO BMDM
721 were treated with highly-oxidized LDL (Hi-ox-LDL, 24 hours) and retained total (TC) and
722 free cholesterol (FC) were quantified. Cholesterol ester (CE), the primary component of
723 lipid droplets was calculated and reported as the difference between TC and FC. mεKO
724 BMDMs contained significantly more TC and CE (Figure 9A). These data utilize a

725 different technique for quantifying lipid while providing an independent but consistent
726 result that expression of PKCε moderates lipid retention by MØ. Indeed, these in vitro
727 results are recapitulated in vivo (i.e, higher ORO staining in mεKO aortic roots;Figure
728 8B).

729 While larger foam cells in mεKO plaques implies more lipid, it is not a direct
730 measure of MØ lipid content. Thus we isolated elicited peritoneal macrophages from
731 mεKO and WT mice that were injected with AAV8-PCSK9 and fed either a chow or high
732 fat diet (4 weeks, Figure 9B). mεKO PMACs, even from animals on a chow diet,
733 contained significantly more lipid droplets than WT (Figure 9C). While a HFD increased
734 lipid retention in both genotypes, retention was substantially higher in mεKO cells
735 (Figure 9C). In conclusion, these data provide in vivo validation of the in vitro results
736 and implicate MØ PKCε in the regulation of regulates lipid dynamics in a way that could
737 slow the progression of atherosclerosis. *How* this occurs is an open question.

738 *RNAseq.* Given that mεKO MØ retain dramatically more lipid than WT, and that lipid
739 loading does not alter SR (Figure 5) or efflux transporter expression (Supplemental
740 Figure S3C,D), we are left with a conundrum: *How* is PKCε regulating lipid dynamics
741 independently of receptor expression? We turned to RNAseq as a discovery based
742 means to provides clues as to PKCε's mechanism of action. We submitted the RNA
743 from pMACs isolated from mεKO and WT mice (Figure 9B) for RNA sequencing and
744 produced the GSE291828 database. Principle Component Analysis (PCA) revealed
745 distinct differences between chow and HFD groups confirming that diet changes gene
746 expression. That there are differences between WT and mεKO HFD animals indicates
747 that genotype is also affecting gene expression (Figure 9D). To determine *how* PKCε

748 may be protective in a hypercholesterolemic environment, we focused on the data from
749 HFD fed mice. A volcano plot reveals 173 genes upregulated and 105 genes down-
750 regulated in hypercholesterolemic mεKO compared to WT. PRKCE is significantly
751 downregulated in mεKO confirming the efficiency/selectivity of our LysM Cre PKCε$^{fl/fl}$
752 model (Figure 9E). Not surprisingly, many of the upregulated gene families include
753 response to bacteria and regulation of immune effector functions, consistent with the
754 fact that the global PKCε knockout mouse succumbs to infections that are cleared by
755 WT mice.[54] Of particular interest is the Gene Ontology (GO) summary family *Import Into*
756 *Cell* (Figure 9F). This family includes genes related to phagocytosis, endocytosis, and
757 receptor-mediated endocytosis (Figure 9G), which dovetails with our previous work
758 demonstrating a role for PKCε in phagocytosis, membrane mobilization, and vesicular
759 trafficking.[12,13] As modified lipids are taken up by endocytosis, and endocytosis would
760 not necessarily require changes in receptor expression, we asked if *endocytosis* is
761 altered in mεKO MØ. To test this, we implemented a model of synchronized endocytosis
762 (30, 60 minutes) using Alexa-488 labeled Ac-LDL. At these early timepoints, mεKO MØ
763 contain significantly more fluorescent endosomes than their WT counterparts (Figure
764 9H) consistent with the hypothesis that PKCε regulates lipid trafficking independent of
765 receptor expression. Further work is needed to elucidate exactly what that pathway is
766 and how it is impacted by expression or absence of PKCε but this body of work is the
767 first to implicate MØ PKCε in restricting/slowing atherosclerosis.
768 In summary, the overall composition of mεKO plaques (larger, more necrotic,
769 engorged foam cells, embedded collagen overlayed with new plaque, and significantly
770 thinner caps) is consistent with human metrics of vulnerability. In addition, RNA

771 sequencing reveal atheroprone mεKO mice have increased expression in genes related
772 to endocytosis and endocytosis studies confirm differences in the amount of
773 endocytosis lipid (Figure 9H). As the mεKO animals have PKCε deletion restricted to
774 myeloid cells, we can conclude that loss of *myeloid* PKCε exacerbates the
775 atherosclerotic program. Conversely, this work identifies myeloid PKCε as a potential
776 atheroprotective gene.
777

778 **DISCUSSION**

779 Knowing that FcR ligation stimulates TNFα release, and that FcR ligation activates
780 PKCε, it was initially surprising that PKCε deletion enhanced TNFα release but had no
781 effect on IL6 (Figure 1B). In contrast, εKO macrophages have blunted responses to
782 LPS/IFNγ, including lower production of NO, TNFα, and IL6. [54] These conflicting results
783 suggest that MØ responses are tuned to their environment, with their signaling
784 response differing if initiated through TLR *vs* FcR. In the context of atherosclerosis, the
785 scale maybe tipped in favor of an FcR activation pathway, based on the elevation of
786 modified LDL-immune complexes in patients with atherosclerosis.[46,47,63] Notably, Murray
787 and Stow[64] reported that secretion of TNFα and IL6 occurs by different pathways in MØ.
788 Although the involvement of PKCε was not addressed, we would postulate that TNFα
789 release involves PKCε signaling while IL6 does not. Furthermore, the fact that εKO
790 secreted significantly more TNFα suggests PKCε expression moderates TNFα
791 secretion, thereby limiting inflammation. According to GSE104140, PKCε expression is
792 significantly decreased in advanced plaques and can be recapitulated in vitro (Figure
793 2B,C). Granted, this is a single database. Extensive searching of the GSE databases

794 turned up one other curated database of human atherosclerotic plaques (GSE120521).
795 The numbers of specimens were low (n=4 stable and 4 unstable). PKCε levels were not
796 significantly different between stable vs unstable plaques. However, it should be noted
797 that these were endarterectomy specimens; disease was already advanced to the point
798 of intervention. With no control to compare, these specimens may reflect the gene
799 signature of the advanced plaques of GSE104140. Indeed, PKCε is significantly lower
800 in both advanced plaque stages of GSE104140 compared to diffuse intimal thickening
801 (Fig 2B) but they are not significantly different from each other (although expression in
802 advanced soft plaques trends lower). However, plaque tissue is a complex mix of cells.
803 Thus, we tested PKCε knockout MØ for lipid uptake and cytokine release in response to
804 FcR ligation (Fig 1). Deletion of PKCε exacerbates both of these metrics and led us to
805 hypothesize that PKCε slows plaque progression.

806 Because PKCε is expressed in many tissues, and modulates such diverse cellular
807 processes as endothelial function, smooth muscle cell migration, proliferation, and
808 inflammation,[24,65,66] determining its role in MØ required generation of a mouse lacking
809 myeloid PKCε. LysM Cre was chosen as it is the most selective and efficient myeloid
810 deletor;[53] the specificity of LysM for PKCε deletion in myeloid cells paralleled that
811 reported for other genes (Figure 3B-D, 4). We exploited the AAV8 PCSK9 + western
812 diet strategy to mimic the hypercholesterolemia produced in humans carrying gain-of-
813 function PCSK9 mutations[51,67] rather than crossing into the more traditional ApoE or
814 LDLR knockout mice.

815 We did note a light PKCε band in pMAC, but not BMDM lysates from mεKO animals
816 (Figure 3C,D) This signal may be from resident peritoneal B-1A cells that express high

817 levels of PKCε (ImmGen Probe Set 10447294). Importantly, we established that, similar
818 to the global PKCε knockout mouse, loss of MØ PKCε does not alter steady state blood
819 composition (Figure 3E-L) or expression of 25 genes linked to atherosclerosis (Figure 5
820 and Supplemental Figures S2-S6). Thus, any differences in the context of
821 hypercholesterolemia can be linked to myeloid PKCε.

822 Having established that plaques from mεKO mice are significantly more advanced
823 than WT, and exhibit markers similar to that of vulnerable human plaques, we turned to
824 lipid loaded MØ to probe mechanism (Figures 6-8). Lipid loading was done either in vivo
825 (pMAC from hypercholesteremic mice) or in vitro (Hi-ox-LDL fed BMDM). Regardless of
826 loading strategy, expression of the cohort of genes was unchanged, yet mεKO retained
827 more TC and CE as well as more lipid droplets compared to control, arguing that PKCε
828 regulates lipid handling but not through these genes (Figures 5, 9A-C).

829 RNAseq of pMAC isolated from hypercholesterolemic WT and mεKO mice provided
830 a discovery-based approach to uncover potential signaling pathways impacted by PKCε
831 expression. Consistent with results from the global knockout mouse, response to
832 bacterium was dramatically upregulated in lipid loaded mεKO pMAC (Figure 9F).
833 Potentially relevant to atherosclerosis are signaling pathways that would facilitate MØ
834 entry into plaques (i.e., cell adhesion, cell motility, locomotion, chronic inflammation,
835 and cytokine signaling). Additionally, upregulation of apoptosis signaling suggests that
836 mεKO MØ may be more sensitive to apoptosis. This is in line with numerous cancer
837 studies in which overexpressed PKCε was found to be anti-apoptotic.[32-37] Notably,
838 increased MØ apoptosis in plaques can lead to necrosis which is higher in mεKO
839 plaques (Figure 8).

840 That loss of PKCε results in more lipid retention was validated in BMDM from mεKO
841 and εKO mice and in pMACs isolated from hypercholesterolemic mice (Figures 1,9).
842 This could theoretically be extended to humans as PKCε is lower in advanced plaques
843 (Figure 2B). However, with no change in SR expression (Figure 5) and no apparent
844 difference in expression of the efflux transporters ABCA1 and ABCG1 (Supplemental
845 Figure S3C,D), we are left to consider PKCε signaling. We know that PKCε controls
846 vesicular trafficking for membrane expansion during FcR mediated phagocytosis.[12,68]
847 Most lipid loading experiments rely on long term (4-72 hours) incubations for lipid
848 droplet assessment and uptake typically occurs by receptor mediated endocytosis. To
849 compliment this, RNA sequencing revealed the GO families *Import into Cell* and
850 *Endocytosis* to be significantly upregulated in mεKO pMAC from hypercholesterolemic
851 mice (Figure 9F,G). To test the hypothesis that endocytosis may be elevated in mεKO
852 MØ, we followed uptake of A488 labeled Ac-LDL for 30 and 60 minutes. At these early
853 timepoints mεKO MØ were significantly more fluorescent that their WT counterparts
854 (Figure 9H), consistent with enhanced endocytosis.
855 Given no change in receptor expression, our data suggests PKCε acts on an
856 intracellular signaling network; its loss leads to increased lipid retention. But, we know
857 that PKCε regulates vesicle delivery from Golgi to phagosomes and that vesicles are
858 not delivered in PKCε null MØ.[12,68] How then, do we explain the apparent disparity, its
859 loss decreases vesicle trafficking to the plasma membrane in phagocytosis but
860 increases lipid uptake during hypercholesterolemia? One possibility is that PKCε
861 functions at a trafficking node to move vesicles along microtubules. During
862 phagocytosis, it brings Golgi-derived vesicles to the phagosome and phosphorylates

863 proteins necessary for vesicle fusion.[12] It may facilitate endocytosis by regulating
864 trafficking and/or fusion along the maturation path. Its loss may interrupt endosome
865 maturation, allowing accumulation of lipid laden endosomes and ultimately, larger foam
866 cells. That mεKO MØ have more endosomes after 30 minutes of lipid loading (Figure
867 9H), retain more TC and CE (Figure 9A), and lipid droplets after lipid loading (Figure
868 9C), is consistent with such a model. While requiring a rigorous test of the hypothesis,
869 this work provides a framework for studies going forward.
870 In conclusion, we generated and characterized the mεKO mouse with
871 PKCε selectively and efficiently deleted in myeloid cells. Utilizing the AAV8-PCSK9 +
872 western diet strategy, we established that mεKO mice have more advanced plaques
873 with markers (e.g. thin/no collagen caps, more necrosis, cholesterol clefts) reminiscent
874 of vulnerable human plaques. mεKO MØ retain more lipid despite no differences in
875 expression of SR or ABCA1 ABCG1. RNAseq results highlight endocytosis as a
876 signaling pathway upregulated in MØ from hypercholesterolemic animals and
877 endocytosis is significantly elevated in mεKO MØ. Together, these results are the first to
878 report a protective role for PKCε in atherogenesis. The reduction of PKCε in advanced
879 human plaques suggests that strategies to retain PKCε expression may represent a
880 novel therapeutic approach to limit atherosclerosis and the medical conditions
881 associated with cardiovascular disease. Our ongoing challenge is to determine the
882 mechanism of PKCε protection and why it decreases as atherosclerosis progresses.
883
884 **Acknowledgments**

885 The authors thank Dr. Gabrielle Fredman for her expertise in atherosclerosis and
886 constructive feedback on experimental design, technical training, and data analysis. Dr.
887 Younghwa Goo for help with cholesterol assays. Thank you to Dr. Paul Feustel for
888 aiding in statistical analysis. The authors would also like to thank Genome Editing
889 and Animal Models Core at the University of Wisconsin (Madison) Biotechnology Center
890 for supplying the PKCε$^{fl/fl}$ sperm, Taconic Biosciences (Rensselaer, NY) for producing
891 PKCε$^{fl/fl}$ mice, Cheryl Zjad for doing the initial animal husbandry and aiding in the
892 development of the LysMCre PKCε$^{fl/fl}$ murine line, Rosemary Prestipino for assisting in
893 the creation of the graphical abstract, Albany Medical College's Bioinformatic Core for
894 producing graphs from RNA sequencing data, and BioRender for aiding in diagram
895 development. ATW backcrossed the PKCε$^{fl/fl}$ mice to generate the congenic strain for
896 Jackson Labs (B6(Cg)-*Prkce*$^{tm1.1Akv}$/LennMmjax stock# 69556), maintained the LysM
897 Cre PKCε$^{fl/fl}$ colony, designed and conducted experiments, analyzed the data, and
898 wrote the manuscript. RBR managed and analyzed NCBI's geneset GSE104140 and
899 our GSE291828. MMS processed and analyzed the aortic arch tissue and ran qPCR
900 and western blots. RHB processed MØ and ran qPCR. AED ran and analyzed
901 experiments using the global (εKO) knockout MØ. MRL coordinated the research,
902 provided the funding, ran and analyzed flow cytometry, and edited the manuscript.
903

904 **Sources of Funding**

905 This work was supported by R03 AI144841, R21 AI185827, Johnathan Vasiliou
906 Foundation, and Albany Medical College Bridge Funds.
907

908 **Disclosures**

909 None.

910

911 **Supplemental Material**

912 Figure S1-S7

913 Full unedited gels

914 Major Resources Table
915
916

REFERENCES

1. What is Cardiovascular Disease. https://www.heart.org/en/health-topics/consumer-healthcare/what-is-cardiovascular-disease.
2. Di Cesare M, Perel P, Taylor S, Kabudula C, Bixby H, Gaziano TA, McGhie DV, Mwangi J, Pervan B, Narula J, et al. The Heart of the World. *Glob Heart*. 2024;19:11. doi: 10.5334/gh.1288
3. Heart Disease Facts. CDC Heart Disease. https://www.cdc.gov/heart-disease/data-research/facts-stats/index.html. 2024
4. Liu Y, Yuan J, Tan T, Jia W, Lugea A, Mareninova O, Waldron RT, Pandol SJ. Genetic inhibition of protein kinase Cε attenuates necrosis in experimental pancreatitis. *Am J Physiol Gastrointest Liver Physiol*. 2014;307:G550-563. doi: 10.1152/ajpgi.00432.2013
5. Tabas I, García-Cardeña G, Owens GK. Recent insights into the cellular biology of atherosclerosis. *J Cell Biol*. 2015;209:13-22. doi: 10.1083/jcb.201412052
6. Hafiane A. Vulnerable Plaque, Characteristics, Detection, and Potential Therapies. *J Cardiovasc Dev Dis*. 2019;6. doi: 10.3390/jcdd6030026
7. Bobryshev YV, Ivanova EA, Chistiakov DA, Nikiforov NG, Orekhov AN. Macrophages and Their Role in Atherosclerosis: Pathophysiology and Transcriptome Analysis. *Biomed Res Int*. 2016;2016:9582430. doi: 10.1155/2016/9582430
8. Petersen C, Peçanha PB, Venneri L, Pasanisi E, Pratali L, Picano E. The impact of carotid plaque presence and morphology on mortality outcome in cardiological patients. *Cardiovasc Ultrasound*. 2006;4:16. doi: 10.1186/1476-7120-4-16
9. Kasikara C, Doran AC, Cai B, Tabas I. The role of non-resolving inflammation in atherosclerosis. *J Clin Invest*. 2018;128:2713-2723. doi: 10.1172/jci97950
10. Moore KJ, Tabas I. Macrophages in the pathogenesis of atherosclerosis. *Cell*. 2011;145:341-355. doi: 10.1016/j.cell.2011.04.005
11. Lennartz MR, Aggarwal A, Michaud TM, Feustel PJ, Jones DM, Brosnan MJ, Keller RS, Loegering DJ, Kreienberg PB. Ligation of macrophage Fcγ receptors recapitulates the gene expression pattern of vulnerable human carotid plaques. *PLoS One*. 2011;6:e21803. doi: 10.1371/journal.pone.0021803
12. D'Amico AE, Wong AC, Zajd CM, Zhang X, Murali A, Trebak M, Lennartz MR. PKC-ε regulates vesicle delivery and focal exocytosis for efficient IgG-mediated phagocytosis. *J Cell Sci*. 2021;134:jcs258886. doi: 10.1242/jcs.258886
13. Hanes CM, D'Amico AE, Ueyama T, Wong AC, Zhang X, Hynes WF, Barroso MM, Cady NC, Trebak M, Saito N, et al. Golgi-associated protein kinase C-ε is delivered to phagocytic cups: Role of phosphatidylinositol 4-phosphate. *J Immunol*. 2017;199:271-277. doi: 10.4049/jimmunol.1700243
14. Larsen EC, Ueyama T, Brannock PM, Shirai Y, Saito N, Larsson C, Loegering D, Weber PB, Lennartz MR. A role for PKC-epsilon in Fc gammaR-mediated phagocytosis by RAW 264.7 cells. *J Cell Biol*. 2002;159:939-944. doi: 10.1083/jcb.200205140
15. Wood TR, Chow RY, Hanes CM, Zhang X, Kashiwagi K, Shirai Y, Trebak M, Loegering DJ, Saito N, Lennartz MR. PKC-ε pseudosubstrate and catalytic

activity are necessary for membrane delivery during IgG-mediated phagocytosis. *J Leukoc Biol*. 2013;94:109-122. doi: 10.1189/jlb.1212634

16. Poolman TM, Quinn PA, Ng L. Protein kinase C epsilon contributes to NADPH oxidase activation in a pre-eclampsia lymphoblast cell model. *Diseases*. 2013;1:1-17. doi: 10.3390/diseases1010001
17. Reyland ME. Protein kinase C isoforms: Multi-functional regulators of cell life and death. *Front Biosci (Landmark Ed)*. 2009;14:2386-2399. doi: 10.2741/3385
18. Larsen EC, DiGennaro JA, Saito N, Mehta S, Loegering DJ, Mazurkiewicz JE, Lennartz MR. Differential requirement for classic and novel PKC isoforms in respiratory burst and phagocytosis in RAW 264.7 cells. *J Immunol*. 2000;165:2809-2817. doi: 10.4049/jimmunol.165.5.2809
19. Crane MJ, Daley JM, van Houtte O, Brancato SK, Henry WL, Jr., Albina JE. The monocyte to macrophage transition in the murine sterile wound. *PLoS One*. 2014;9:e86660. doi: 10.1371/journal.pone.0086660
20. Tabas I. Macrophage apoptosis in atherosclerosis: consequences on plaque progression and the role of endoplasmic reticulum stress. *Antioxid Redox Signal*. 2009;11:2333-2339. doi: 10.1089/ars.2009.2469
21. Fredman G, Li Y, Dalli J, Chiang N, Serhan CN. Self-limited versus delayed resolution of acute inflammation: temporal regulation of pro-resolving mediators and microRNA. *Sci Rep*. 2012;2:639. doi: 10.1038/srep00639
22. Chen L, Shi D, Guo M. The roles of PKC-d and PKC-e in myocardial ischemia/reperfusion injury. *Pharmacol Res*. 2021;170:105716
23. Zuniga MC, Raghuraman G, Hitchner E, Weyand C, Robinson W, Zhou W. PKC-epsilon and TLR4 synergistically regulate resistin-mediated inflammation in human macrophages. *Atherosclerosis*. 2017;259:51-59. doi: 10.1016/j.atherosclerosis.2017.02.021
24. Inagaki K, Churchill E, Mochly-Rosen D. Epsilon protein kinase C as a potential therapeutic target for the ischemic heart. *Cardiovasc Res*. 2006;70:222-230. doi: 10.1016/j.cardiores.2006.02.015
25. Palaniyandi SS, Sun L, Ferreira JC, Mochly-Rosen D. Protein kinase C in heart failure: a therapeutic target? *Cardiovasc Res*. 2009;82:229-239. doi: 10.1093/cvr/cvp001
26. Saurin AT, Pennington DJ, Raat NJH, Latchman DS, Owen MJ, Marber MS. Targeted disruption of the protein kinase C epsilon gene abolishes the infarct size reduction that follows ischaemic preconditioning of isolated buffer-perfused mouse hearts. *Cardiovasc Res*. 2002;55:672-680
27. Lien CF, Chen SJ, Tsai MC, Lin CS. Potential role of protein kinase C in the pathophysiology of diabetes-associated atherosclerosis. *Front Pharmacol*. 2021;12:716332. doi: 10.3389/fphar.2021.716332
28. Waza AA, Andrabi K, Hussain MU. Protein kinase C (PKC) mediated interaction between conexin43 (Cx43) and K(+)(ATP) channel subunit (Kir6.1) in cardiomyocyte mitochondria: Implications in cytoprotection against hypoxia induced cell apoptosis. *Cell Signal*. 2014;26:1909-1917. doi: 10.1016/j.cellsig.2014.05.002

1007 29. Singh RK, Haka AS, Asmal A, Barbosa-Lorenzi VC, Grosheva I, Chin HF, Xiong
1008 Y, Hla T, Maxfield FR. TLR4 (Toll-Like Receptor 4)-dependent signaling drives
1009 extracellular catabolism of LDL (Low-Density Lipoprotein) aggregates.
1010 *Arterioscler Thromb Vasc Biol*. 2020;40:86-102. doi:
1011 10.1161/atvbaha.119.313200
1012 30. Faisal A, Saurin A, Gregory B, Foxwell B, Parker PJ. The scaffold MyD88 acts to
1013 couple protein kinase Cepsilon to Toll-like receptors. *J Biol Chem*.
1014 2008;283:18591-18600. doi: 10.1074/jbc.M710330200
1015 31. Ross AM, Gibbons RJ, Stone GW, Kloner RA, Alexander RW. A randomized,
1016 double-blinded, placebo-controlled multicenter trial of adenosine as an adjunct to
1017 reperfusion in the treatment of acute myocardial infarction (AMISTAD-II). *J Am*
1018 *Coll Cardiol*. 2005;45:1775-1780. doi: 10.1016/j.jacc.2005.02.061
1019 32. Gorin MA, Pan Q. Protein kinase C epsilon: an oncogene and emerging tumor
1020 biomarker. *Mol Cancer*. 2009;8:9. doi: 10.1186/1476-4598-8-9
1021 33. He S, Li Q, Huang Q, Cheng J. Targeting Protein Kinase C for Cancer Therapy.
1022 *Cancers (Basel)*. 2022;14:1104. doi: 10.3390/cancers14051104
1023 34. Casado-Medrano V, Baker M, J., Cooke M, Kazanietz MG. Mechanisms of
1024 protein kinase C epsilon down-regulation by transforming growth factor-beta in
1025 lung cancer cells. *bioR$_x$iv*. 2020:2. doi: https://doi.org/10.1101/2020.10.28.359588

35. Nicholson R, Menezes AC, Azevedo A, Leckenby A, Davies S, Seedhouse C, Gilkes A, Knapper S, Tonks A, Darley RL. Protein kinase C epsilon overexpression is associated with poor patient outcomes in AML and promotes Daunorubicin resistance through p-glycoprotein-mediated drug efflux. *Front Oncol*. 2022;12:840046
36. Sivaprasad U, Shankar E, Basu A. Downregulation of Bid is associated with PKCepsilon-mediated TRAIL resistance. *Cell Death Differ*. 2007;14:851-860. doi: 10.1038/sj.cdd.4402077
37. Huang B, Cao K, Li X, Guo S, Mao X, Wang Z, Zhuang J, Pan J, Mo C, Chen J, et al. The expression and role of protein kinase C (PKC) epsilon in clear cell renal cell carcinoma. *J Exp Clin Cancer Res*. 2011;30:88
38. Poznyak AV, Sukhorukov VN, Guo S, Postnov AY, Orekhov AN. Sex Differences Define the Vulnerability to Atherosclerosis. *Clin Med Insights Cardiol*. 2023;17:11795468231189044. doi: 10.1177/11795468231189044
39. Wang S, Lai X, Deng Y, Song Y. Correlation between mouse age and human age in anti-tumor research: Significance and method establishment. *Life Sci*. 2020;242:117242. doi: 10.1016/j.lfs.2019.117242
40. Diaz Brinton R. Minireview: translational animal models of human menopause: challenges and emerging opportunities. *Endocrinology*. 2012;153:3571-3578. doi: 10.1210/en.2012-1340
41. Vozenilek AE, Blackburn CMR, Schilke RM, Chandran S, Castore R, Klein RL, Woolard MD. AAV8-mediated overexpression of mPCSK9 in liver differs between male and female mice. *Atherosclerosis*. 2018;278:66-72. doi: 10.1016/j.atherosclerosis.2018.09.005
42. Nakashima Y, Wright TN, Sueishi K. Early atherosclerosis in humans: role of diffuse intimal thickening and extracellular matrix proteoglycans. *Cardiovasc Res*. 2008;79:14-23. doi: 10.1093/cvr/cvn099
43. Harmon EY, Fronhofer V, 3rd, Keller RS, Feustel PJ, Zhu X, Xu H, Avram D, Jones DM, Nagarajan S, Lennartz MR. Anti-inflammatory immune skewing is atheroprotective: Apoe−/−FcγRIIb−/− mice develop fibrous carotid plaques. *J Am Heart Assoc*. 2014;3:e001232. doi: 10.1161/jaha.114.001232
44. Barra J, Crosbourne I, Roberge CL, Bossardi-Ramos R, Warren JSa, Matteson K, Wang L, Jourd'heuil F, Borisov SM, Bresnahan E, et al. DMT1-dependent endosome-mitochondria interactions regulate mitochondrial iron translocation and metastatic outgrowth. *Oncogene*. 2024;43:650-667.
45. Lopes-Virella MF, Virella G. Pathogenic role of modified LDL antibodies and immune complexes in atheroslcerosis. *J Atheroscler Thromb*. 2013;20:743-754. doi: 10.5551/jat.19281
46. Sobenin IA, Salonen JT, Zhelankin AV, Melnichenko AA, Kaikkonen J, Bobryshev YV, Orekhov AN. Low density lipoprotein-containing circulating immune complexes: role in atherosclerosis and diagnostic value. *Biomed Res Int*. 2014;2014:205697. doi: 10.1155/2014/205697
47. Wolf D, Ley K. Immunity and Inflammation in Atherosclerosis. *Circ Res*. 2019;124:315-327. doi: 10.1161/circresaha.118.313591
48. Nakashima Y, Fujii G, Sumiyoshi S, Wright TN, Sueishi K. Early human atherosclerosis: accumulation of lipid and proteoglycans in intimal thickenings

1072 followed by macrophagbe infiltration. *Arterioscler Thromb Vasc Biol*.
1073 2007;27:1159-1165. doi: 10.1161/ATVBAHA.106.134080
1074 49. Kolodgie FD, Burke AP, Nakazawa G, Virmani R. Is pathological intimal
1075 thickening the key to understanding early plaque progression in human
1076 atherosclerotic disease? *Art Thromb Vasc Biol*. 2007;27:986-989. doi:
1077 10.1161.ATV.0000258865.44774.41
1078 50. Transcriptome sequencing of human fibroatheromas identifies genetic signature
1079 of plaque formation and suggests roles of TREM1 and PIK3CG in
1080 atherosclerosis.
1081 https://www.ncbi.nlm.nih.gov/geo/query/acc.cgi?acc=GSE104140. 2020
1082 51. Keeter WC, Carter NM, Nadler JL, Galkina EV. The AAV-PCSK9 murine model of
1083 atherosclerosis and metabolic dysfunction. *Eur Heart J Open*. 2022;2:oeac028.
1084 doi: 10.1093/ehjopen/oeac028
1085 52. Hafeez BB, Zhong W, Weichert J, Dreckschmidt NE, Jamal MS, Verma AK.
1086 Genetic ablation of PKC epsilon inhibits prostate cancer development and
1087 metastasis in transgenic mouse model of prostate adenocarcinoma. *Cancer Res*.
1088 2011;71:2318-2327. doi: 10.1158/0008-5472.Can-10-4170
1089 53. Abram CL, Roberge GL, Hu Y, Lowell CA. Comparative analysis of the efficiency
1090 and specificity of myeloid-Cre deleting strains using ROSA-EYFP reporter mice. *J*
1091 *Immunol Methods*. 2014;408:89-100. doi: 10.1016/j.jim.2014.05.009
1092 54. Castrillo A, Pennington DJ, Otto F, Parker PJ, Owen MJ, Boscá L. Protein kinase
1093 Cepsilon is required for macrophage activation and defense against bacterial
1094 infection. *J Exp Med*. 2001;194:1231-1242. doi: 10.1084/jem.194.9.1231
1095 55. Schaap D, Parker PJ, Bristol A, Kriz R, Knopf J. Unique substrate specificity and
1096 regulatory properties of PKC-epsilon: a rationale for diversity. *FEBS Lett*.
1097 1989;243:351-357. doi: 10.1016/0014-5793(89)80160-7
1098 56. Stöger JL, Gijbels MJ, van der Velden S, Manca M, van der Loos CM, Biessen
1099 EA, Daemen MJ, Lutgens E, de Winther MP. Distribution of macrophage
1100 polarization markers in human atherosclerosis. *Atherosclerosis*. 2012;225:461-
1101 468. doi: 10.1016/j.atherosclerosis.2012.09.013
1102 57. Xu M, Wu X, Liu Z, Ding Y, Kong W, Little PJ, Xu S, Weng J. A novel mouse
1103 model of diabetes, atherosclerosis and fatty liver disease using an AAV8-PCSK9-
1104 D377Y injection and dietary manipulation in db/db mice. *Biochem Biophys Res*
1105 *Commun*. 2022;622:163-169. doi: 10.1016/j.bbrc.2022.07.031
1106 58. Getz G, Reardon CA. Animal models of atherosclerosis. *Arterioscler Thromb*
1107 *Vasc Biol*. 2012;32:1104-1115
1108 59. Grebe A, Latz E. Cholesterol crystals and inflammation. *Curr Rheumatol Rep*.
1109 2013;15:313
1110 60. Nadkarni SK, Pierce MC, Park BH, de Boer JF, Whittaker P, Bouma BE, Bressner
1111 JE, Halpern E, Houser SL, Tearney GJ. Measurement of collagen and smooth
1112 muscle cell content in atherosclerotic plaques using polarization-sensitive optical
1113 coherence tomography. *J Am Coll Cardiol*. 2007;49:1474-1481
1114 61. Libby P. Inflammation during the life cycle of the atherosclerotic plague.
1115 *Cardiovasc Res*. 2021;117:2525-2536
1116 62. Lennartz MR, Aggarwal A, Michaud TM, Feustel PJ, Jones DM, Brosnan MJ,
1117 Keller RS, Loegering DJ, Kreienberg PB. Ligation of macrophage Fcy receptors

1118 recapitulates the gene expression pattern of vulnerable human carotid plaques.
1119 *PLoS One* 2011;6:e21803
1120 63. Lopes-Virella MF, Binzafar N, Rackley S, Takei A, La Via M, Virella G. The uptake
1121 of LDL-IC by human macrophages: predominant involvement of the Fc gamma
1122 RI receptor. *Atherosclerosis*. 1997;135:161-170. doi: 10.1016/s0021-
1123 9150(97)00157-3
1124 64. Murray RZ, Stow JL. Cytokine Secretion in Macrophages: SNAREs, Rabs, and
1125 Membrane Trafficking. *Front Immunol*. 2014;5:538. doi:
1126 10.3389/fimmu.2014.00538
1127 65. Ringvold HC, Khalil RA. Protein Kinase C as Regulator of Vascular Smooth
1128 Muscle Function and Potential Target in Vascular Disorders. *Adv Pharmacol*.
1129 2017;78:203-301. doi: 10.1016/bs.apha.2016.06.002
1130 66. Capuani B, Pacifici F, Pastore D, Palmirotta R, Donadel G, Arriga R, Bellia A, Di
1131 Daniele N, Rogliani P, Abete P, et al. The role of epsilon PKC in acute and
1132 chronic diseases: Possible pharmacological implications of its modulators.
1133 *Pharmacol Res*. 2016;111:659-667. doi: 10.1016/j.phrs.2016.07.029
1134 67. Cui Yf, Chen Xc, Mijiti T, Abudurusuli A, Deng Lh, Ma X, Chen B. PCSK9 with a
1135 gain of function D374Y mutation aggravates atheroslcerosis by inhibiting PPARa
1136 expression. *Scientific Reports*. 2025;15
1137 68. D'Amico AE, Lennartz MR. Protein kinase C-epsilon in membrane delivery during
1138 phagocytosis. *J Immunol Sci*. 2018;2:26-32
1139
1140

1141 **Highlights:**

1142 - A novel murine model in which PKCε is floxed (PKCε$^{fl/fl}$) on both alleles haas
1143 been generated, backcrossed, and deposited into Jackson Laboratories
1144 (B6(Cg)- *Prkce*$^{tm1.1Akv}$/LennMmjax). Then, PKCε$^{fl/fl}$ LysM Cre (mεKO) mice have
1145 been generated.
1146 - Deletion of PKCε has no basal affects on other PKC isoforms, lipid handling
1147 markers, or inflammatory markers.
1148 - Upon (in vitro) lipid loading of BMDM or isolating lipid loaded pMACs from
1149 hypercholesterolemic mice (in vivo), mεKO BMDMs retain more cholesterol.
1150 - Long term (16 wk) hypercholesterolemis generates larger lesions, more necrosis,
1151 and thinner plaque caps (i.e., a more vulnerable plaque phenotype) in mεKO
1152 mice.
1153 - RNA sequencing suggests PKCε regulates endocytosis mechanisms post initial
1154 uptake of LDL and has been confirmed in a model of synchronized endocytosis.
1155 - These findings identify myeloid PKCε as a novel atheroprotective molecule
1156 whose expression impacts multiple metrics of atherosclerosis. This opens new
1157 avenues of investigation to uncover the PKCε signaling network responsible for
1158 the phenotype. Understanding how myeloid PKCε slows atherosclerosis
1159 development will aid in the development of novel preventative and therapeutic
1160 treatments.

1161

1162

1163

1164

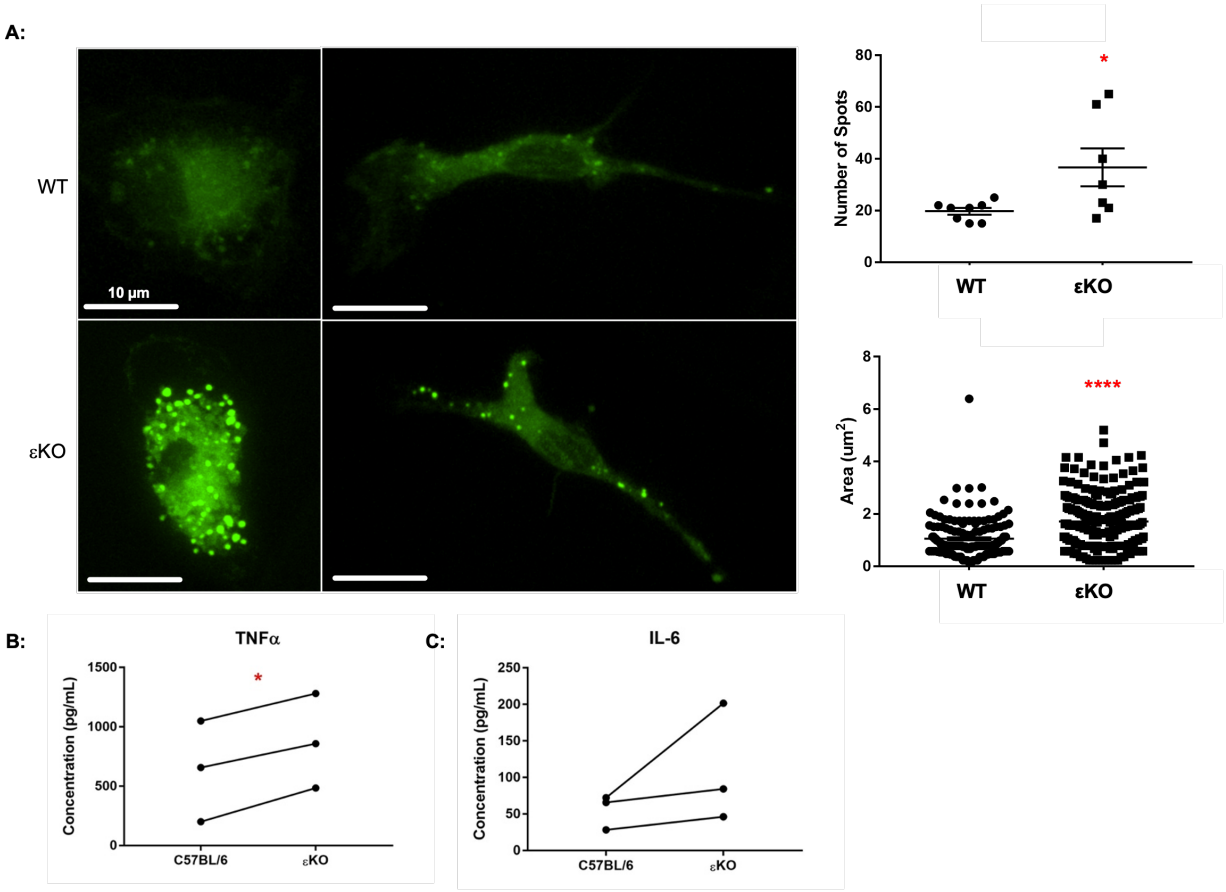

Figure 1: MØ from global PKCε knockout (εKO) mice retain more/larger lipid droplets and release more TNFα. (**A**) C57BL/6 and εKO BMDM were treated with AcLDL (360 µM) for 4h, fixed and lipid droplets stained with BODIPY. Z-stacks were collected, 3-D reconstructions made, and number of lipid droplets and droplet area was quantified (each symbol represents one cell/droplet n = 3 independent experiments). Data are presented as ± SEM. (**B**,**C**) C57BL/6 and εKO BMDM were incubated with or without immune complexes (2 h). Media was collected and TNFα and IL-6 was quantified by ELISA. Net TNFα and IL-6 release is represented (n = 3). Statistical analysis was preformed by two-tailed unpaired t-test (**A**) and two-tailed paired t-test in (**B**,**C**). Scale bars: 10 µm. *$p < 0.05$; ****$p < 0.0001$.

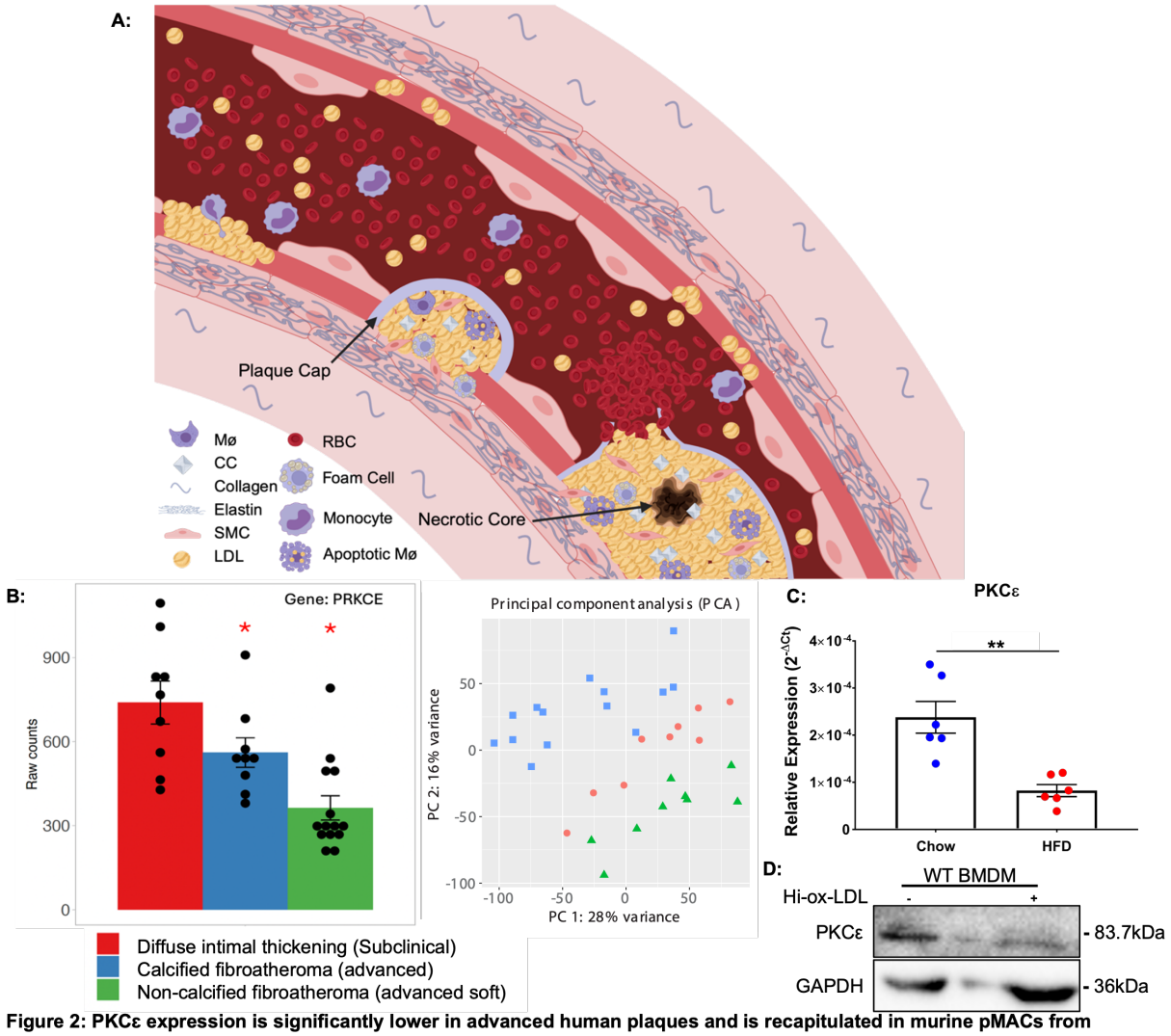

Figure 2: PKCε expression is significantly lower in advanced human plaques and is recapitulated in murine pMACs from hypercholesterolemic mice. (**A**) Schematic of atherogenesis. Created in BioRender. Wells, A. (2024) https://BioRender.com/ b96z554. (**B**) RNAseq of human atherosclerotic plaques (GSE104140) plotting PRKCE raw counts (left) and the corresponding principal component analysis (PCA) (right) (n = 9-14 samples). (**C**) qPCR of PKCε in elicited pMACs from chow and HFD fed WT mice administered with AAV8-PCSK9 for 4-wks (n=3). (**D**) Western blot of BMDM treated with Hi-ox-LDL (50 µg/mL, 24h). Data are presented as ± SEM. Statistical analysis was performed by Limma-voon differential expression analysis (**B**) and two-tailed unpaired t-test (**C**). $^{**}p < 0.01$.

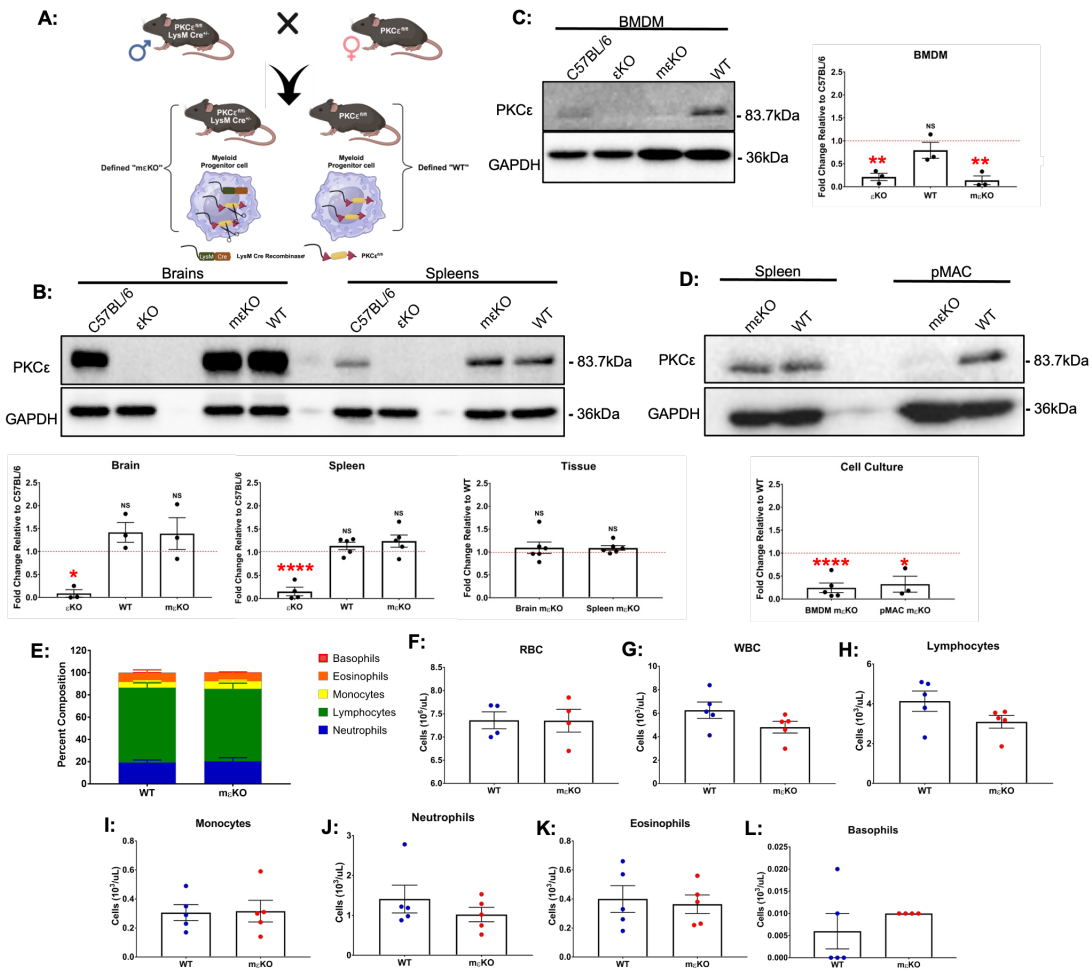

Figure 3: LysM Cre deletes PKCε selectively from myeloid cells and does not affect blood composition. (**A**) Schematic of the LysM Cre PKCε$^{fl/fl}$ breeding strategy. **(B-D)** Representative Western blot and corresponding densitometry of PKCε and GAPDH expression in brains and spleens (**B**), BMDMs **(C)**, and pMACs **(D)** (n=3-6). Tissues from the global PKCε knockout mouse (εKO) are included for reference; ratios of expression. No substantive reduction in PKCε expression was detected in brains or spleens of LysMCre expressers; little/no PKCε was detected in lysates from BMDMs or pMACs expressing Cre. (**E-L**) Blood was collected and analyzed with a Heska HT5 CBC analyzer. (**E**) Composition of total white blood cells (WBC). Total numbers of (**F**) Red blood cells (RBC), (**G**) WBC, (**H**) Lymphocytes, (**I**) Monocytes, (**J**) Neutrophils, (**K**) Eosinophils, and (**L**) Basophils are shown. Data are presented as mean ± SEM. Statistical analysis was performed by two-tailed unpaired t-test (**B**,**D**,**F-L**) and one-way ANOVA (**B**,**C**,**E**) Red dotted line indicates respective C57BL/6 or WT (ie, PKCε$^{fl/fl}$) used as the normalization control. Each symbol represents an individual mouse. *$p < 0.05$; **$p < 0.001$; ****$p < 0.0001$.

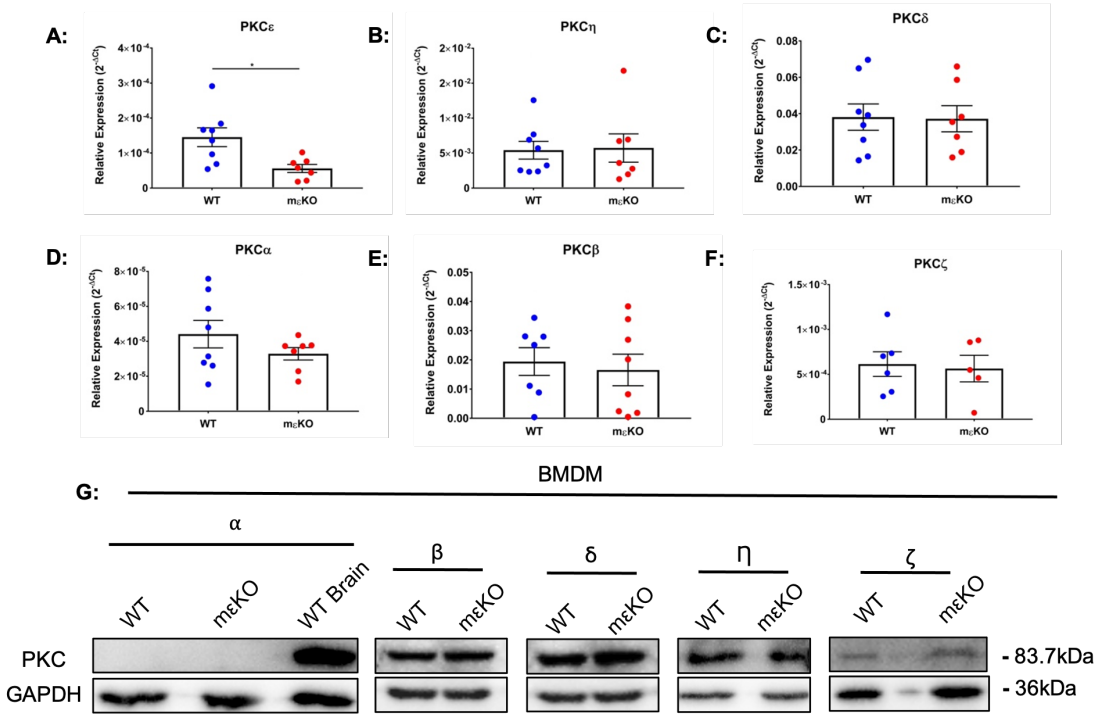

Figure 4: LysM Cre PKCε$^{fl/fl}$ selectively deletes PKCε in MØ. (**A**) qPCR for novel (PKCε, PKCΗ, PKCδ), conventional (PKCα, PKCβ), and atypical (PKCζ) PKC's reveal a significant decrease in PKCε with no effect on other isoforms. (n = 5-8, each symbol represents cells from a single animal). (G) Representative westerns confirming that PKCε deletion does not alter protein expression of other isoforms. (n=3). Data are presented as mean ± SEM. Statistical analysis was performed by two-tailed unpaired t-test in. *$p < 0.05$.

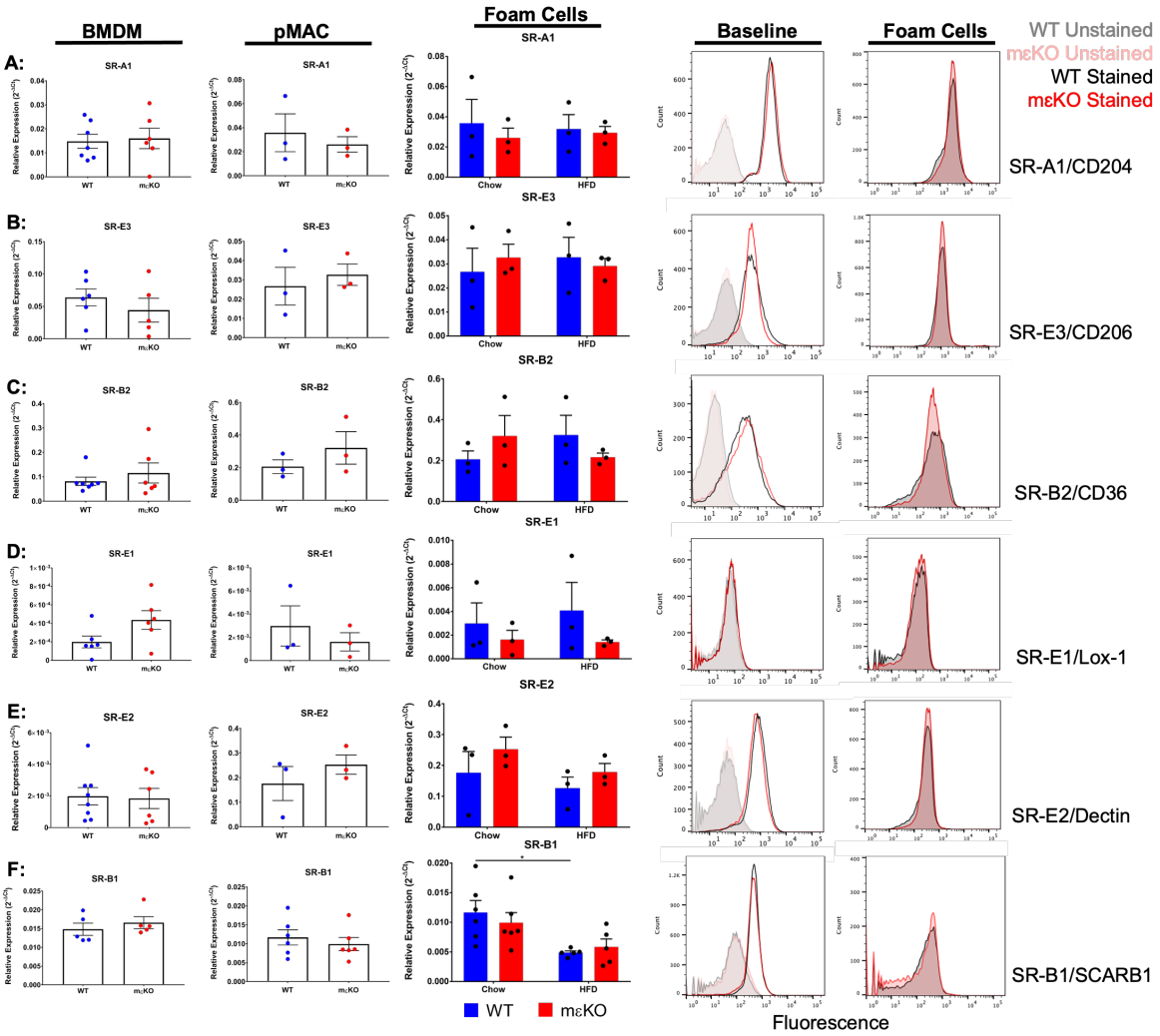

Figure 5: Deletion of PKCε does not alter scavenger receptor expression. (**A-F**) qPCR and flow cytometry for SR-AI (CD204), SR-E3 (CD206), SR-B2 (CD36), SR-E1 (Lox-1), SR-E2 (Dectin-1), and SR-B1 (SCARB1) in BMDMs (column 1,4) and elicited pMACs (column 2) at steady state (each symbol represents an individual animal, n = 3-6). In vivo derived foam cells (column 3, see Methods): qPCR of SR from elicited pMACs. In vitro derived foam cells (column 5): flow cytometry of SR receptors from BMDM loaded with Hi-oxLDL (50 µg/ml, 24 h). Flow cytometry are representative of 3-5 independent experiments. Data are presented as mean ± SEM. Statistical analysis was performed by two-tailed unpaired t-test and two-way ANOVA (there were no significance difference in expression between genotype).

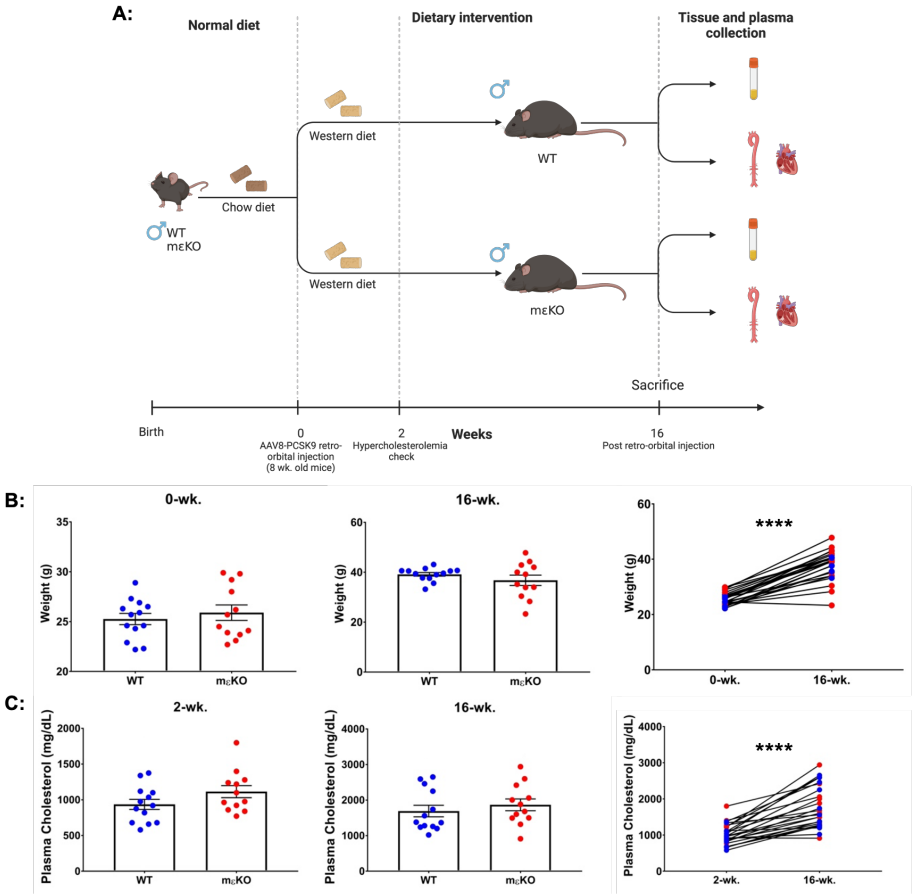

Figure 6: WT and mεKO animals have similar weights and plasma cholesterol levels in an in vivo model of hypercholesterolemia. (**A**) Timeline of in vivo model. Created in BioRender. Wells, A. (2024) https://BioRender.com/ e98l871. (**B**) Weights were recorded at T = 0 and T = 16 wks. Genotype did not affect weight gain. (**C**) Blood was collected at 2 and 16 weeks for determination of plasma cholesterol concentrations. While cholesterol increased over the time course, there was no genotype difference. Each symbol (blue-WT, red-mεKO) represents one animal (n =12-13, two independent cohorts). Data are presented as mean ± SEM. Statistical analysis was performed by two-tailed paired t-tests (**B,C**) and unpaired t-tests (**B,C**). ****$p < 0.0001$.

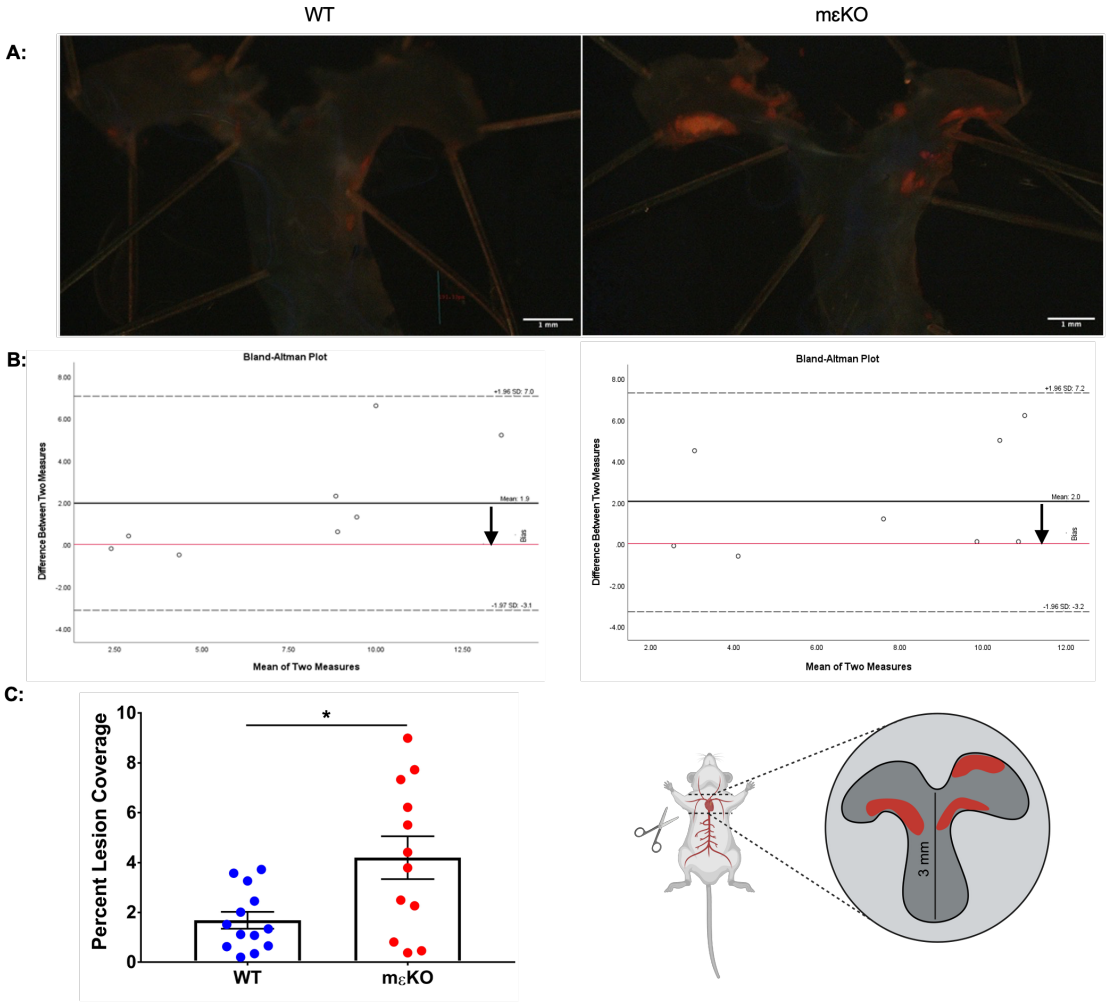

Figure 7: mεKO aortic arches have a higher percent lesion coverage than their WT counterparts. (**A**) Schematic of the region of descending aorta removed; area analyzed is enlarged. Created in BioRender. Wells, A. (2024) https://BioRender.com/ q65k186. Representative images of Oil red O stained *en face* preparations of aortic arches recovered from animals after 16 weeks of hypercholesterolemia. (**B**) A subset of (8) mice were assessed for inter-observer variability, no shift in the bias was detected. (**C**) Quantitation of the aortic arch and 3 mm of descending aorta for percent lesion coverage (n = 12-13, each point represents one animal). See methods for details. Data are presented as mean ± SEM. Statistical analysis was performed by Bland-Altman analysis in (**B**) and two-tailed unpaired t-test in (**C**). Scale Bars: 1 mm. *$p < 0.05$.

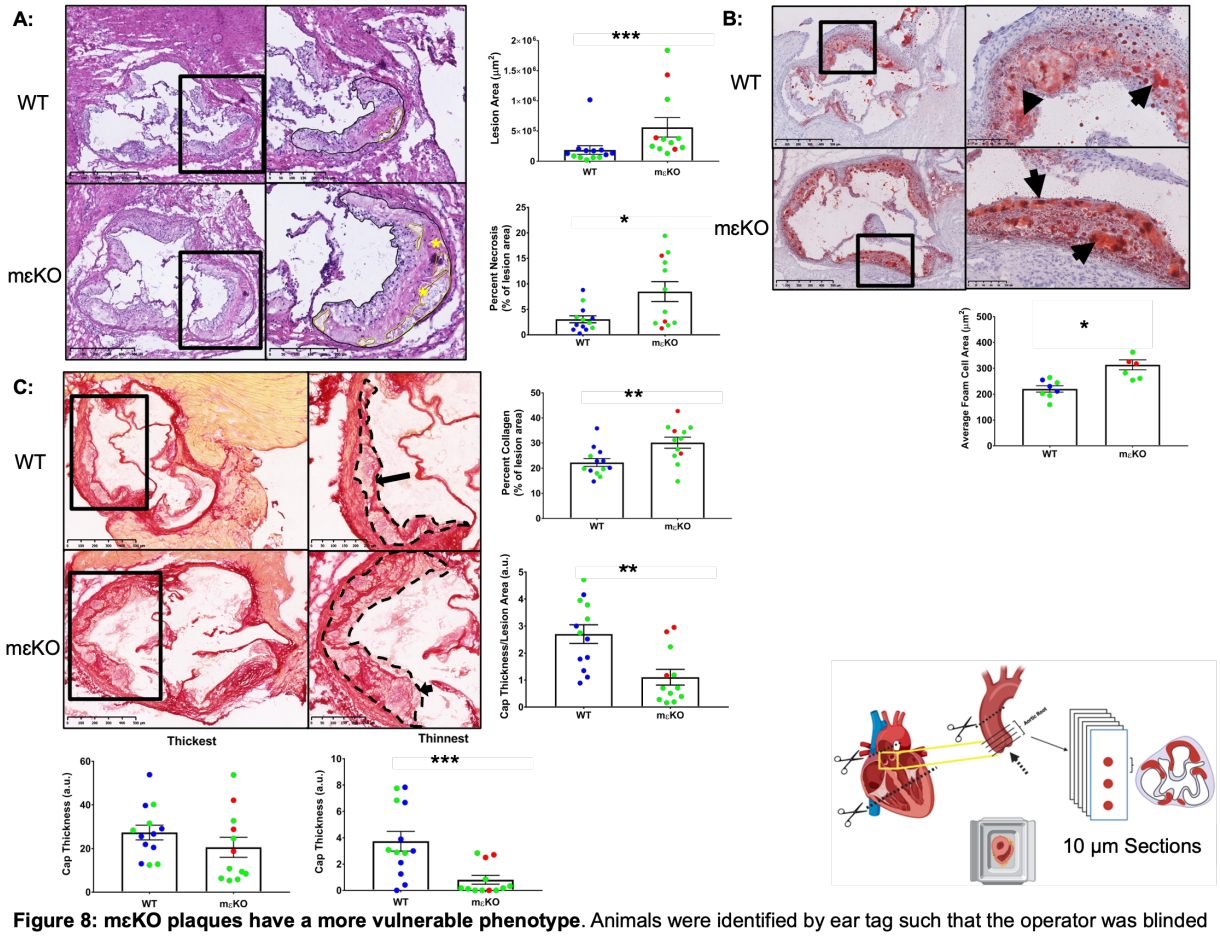

Figure 8: mεKO plaques have a more vulnerable phenotype. Animals were identified by ear tag such that the operator was blinded to genotype until all data was collected (n=12-13/genotype, 2 independent cohorts). See methods for processing/staining details. (**Bottom right**) Schematic of aortic root processing. Created in BioRender. Wells, A. (2024) https://BioRender.com/ f19i190. (**A**) H&E staining: Plaques (black outlined), necrotic regions (yellow outlined) and cholesterol clefts (yellow asterisk) were identified and lesion area and percent necrosis per mouse were quantified. Plaques from mεKO mice were significantly larger and more necrotic. (**B**) Slides consecutive to H&E were stained with ORO and the average foam cell area per mouse was recorded; foam cells (black arrowheads) are significantly larger in mεKO plaques (n = 7-8). (**C**) Plaque sections were stained for collagen with Sirius Red, were outlined (black hashed lines) and overall collagen content reported as a percent of plaque area. As vulnerable plaques have thin collagen caps, we measured the average cap thickness per mouse as well as the thickest and thinnest regions; mεKO plaques have significantly thinner regions than their WT controls; arrow denotes a plaque with a cap and arrowhead denotes a plaque with no cap. (n = 12-13). (**A**,**C**) Scale bars: 500 μm (left) or 250 μm (right). (**B**) Scale bars: 500 μm (left) or 100 μm (right). Each symbol represents one animal and green symbols represent animals that are genotypically ZsGreen Positive. Data are presented as mean ± SEM. Statistical analysis was performed by two-tailed unpaired t-test in. *$p < 0.05$; **$p < 0.01$; *** $p < 0.001$.

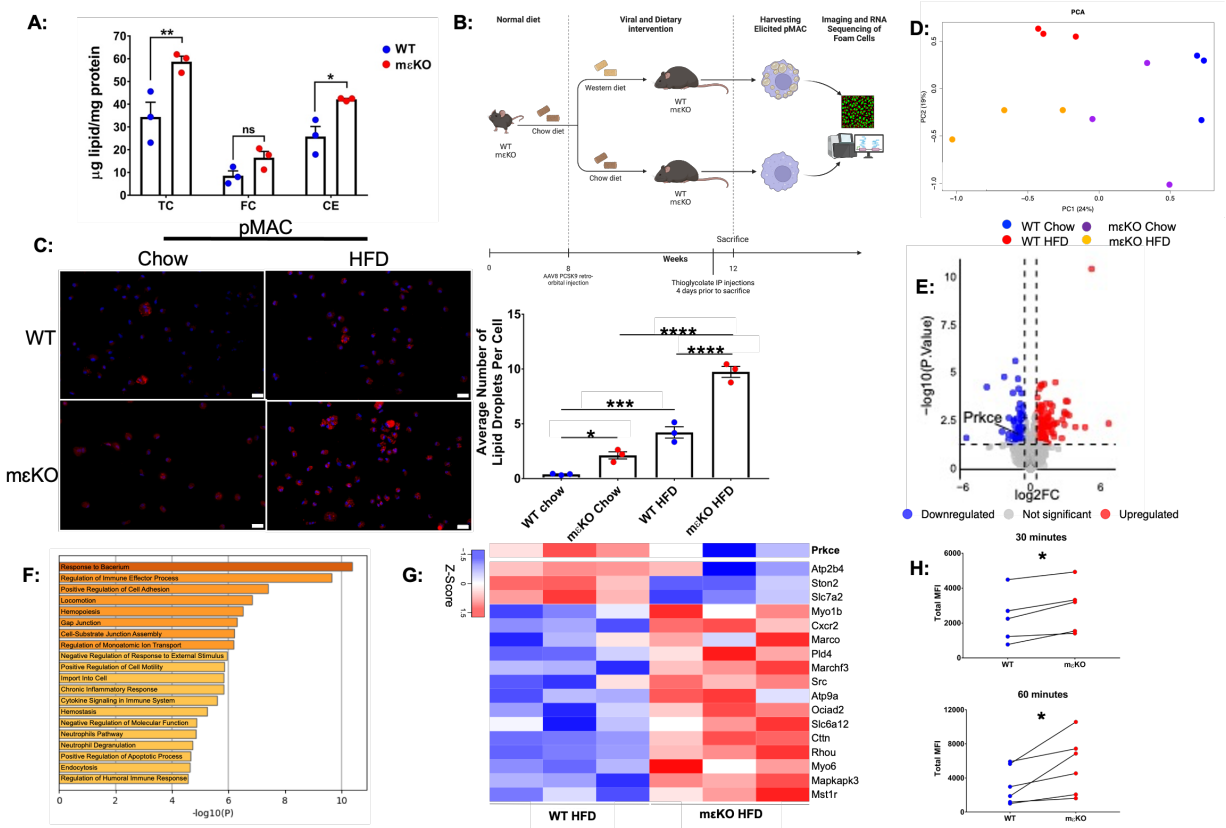

Figure 9: mεKO BMDMs and elicited pMACs retain more cholesterol/lipids in vitro and in vivo through enhanced endocytosis mechanisms. (**A**) BMDMs were loaded with human Hi-ox-LDL for 24h and assessed for total cholesterol (TC), free cholesterol (FC), and cholesterol esters (CE) (n = 3 with 4 technical replicates per n). (**B**) Strategy for generation of foam cells in. vivo. Created in BioRender. Wells, A. (2025) https://BioRender.com/ f20m105. (**C**) Elicited pMACs from animals in (**B**) were stained with LipidTOX and Dapi to label neutral lipids and nuclei. Scale bar: 1µm. The total number of well-defined lipid droplets was assessed by FIJI, normalized to the total number of nuclei, and reported as the average number of lipid droplets per cell. (**D-G**) RNA sequencing of elicited pMACs from hypercholesterolemic mice revealed significant differences in gene expression. (**D**) Principal component analysis (PCA) indicates distinct gene expression profiles as shown by differential clustering by genotype and diet. (**E**) Volcano plot from total RNA sequencing illustrating differentially regulated genes upon deletion of PKCε in hypercholesterolemic mice, where PRKCE is in relation. P value < 0.05 and fold change log2 > 2. (**F**) Gene Ontology analysis of differentially regulated genes upon PKCε deletion. (**G**) Heatmap of gene expression values for significantly downregulated and upregulated genes for import into the cell (i.e., endocytosis, phagocytosis, and receptor-mediated endocytosis) upon deletion of PKCε. (**H**) Synchronized endocytosis of Alexa-488 Ac-LDL for 30 and 60 minutes and assessed for the total MFI of lipid loaded (green) endosomes. (n = 3). Each point in **A-D,H** represents one animal n = 3-4. Data are presented as mean ± SEM. Statistical analysis was performed by one-way ANOVA (**A**,**C**) or paired t-test (**H**). *$p < 0.05$; **$p < 0.01$; ***$p < 0.001$, ****$p < 0.0001$.